MECHANISM AND CONTROL OF HIGH-INTENSITY-LASER-DRIVEN ION ACCELERATION

by

Teh Lin

A dissertation submitted in partial fulfillment
of the requirements for the degree of
Doctor of Philosophy
(Electrical Engineering)
in The University of Michigan
2005

Doctoral Committee:

Professor Donald P. Umstadter, Chair

Professor Ronald M. Gilgenbach

Professor Duncan G. Steel

Associate Research Scientist Anatoly M. Maksimchuk

To my family,

ACKNOWLEDGEMENTS

This research occurred with a lot of support, help, and guidance. First of all, I would acknowledge my research advisor, Prof. Donald Umstadter. He has always showed the highest interests in my research, provided good suggestions and indicated the bright side of the research. He actually made me feel interested in exploring the high filed science and excited me with plentiful excellent critique and insights. Outside the lab, the volleyball games, the canoe trips, and the tennis skill discussions make me unforgettable. Special thanks and acknowledgment for Dr. Anatoly Maksimchuk, in my first year in the lab, he showed me a lot of basic techniques for optics alignment, experiment design and data analysis. In my last year in Ph.D program, he took responsibility to guild me through all the difficulties I encountered in my thesis writing. Prof. Duncan steel, he, from my qualifying exam through my defense, encouraged me continuing further research. Prof. Ronald Gilgenbach helped me understand the beauty of plasma physics and provided penetrating critiques to help me improve my research quality. Prof. Gerard Mourou, as CUOS director, always provided moral support and encouragement of my research and career. His academic knowledge further help me establish my ambition to pursue more physics of plasma physics. Dr. John Nees also provided a lot of useful experiment tricks and academic knowledge to my research.

The senior graduate student, Kirk Flippo, is the first American to whom I spoke English over ten minutes. I definitely owes a debt of gratitude to him. He put up

with my awkward communication skills at my first year, and taught me the late night experiment night schedule, which I still follow until now. My other High Field Grouper: Dr. Sudeep Banerjee for his generous coffee treats, scientific conversations and encouragements, Rahul Shah and Tony Valenzuela for their companion in M3, also Shouyuan Chen, Matt Rever, Ned Saleh, and Scott Sepke. Thanks to Pascal Rousseau for all the computerizing the electronic help for the experiment instrument. This work would not be made possible without the friendship of Kelly Nash, Vina Wong, and Katherine Korbiak. Special thanks for my Taiwanese mafia troupes. You always save me from the busy experiment life. Especially the support from Po-Ju Lin, I will never forget all your help and thoughtfulness in these four years.

Without the help from all the staff in CUOS and EECS, I would not be able to go through all the paper work, financial difficulties and the VISA problems. Thank you Linda, Serina, Tammy, Deb, Bett, Theresa, and Beth.

Finally, I dedicate this work to family: my Mom, Pi-Chun, Dad, Yuan-Jing, brother, Ho, sister-in-law, Mindy, my niece, Grace and Yin-Ming Kuo. Your patience to listen to my complains of my work, support of my life and love made this impossible task happen. Thank you. Thank you so much.

This thesis was formatted using LATEX, compiled by Miktex and written in the Winedit text editor.

TABLE OF CONTENTS

LIST OF FIGURES

Figure

CHAPTER I

Introduction

1.1 Thesis Perspectives

Physicists are always interested in new and unknown topics. In 1927, the Nobel prize-winning American chemist, Irving Langmuir, first used the term "plasma," which in Greek means "moldable substance" or "jelly," to describe an ionized gas; Langmuir noticed the way blood plasma carries red and white corpuscles similar to the way an electrified fluid carries electrons and ions. This moment started a new chapter of physics.

The ordinary matters have a fourth steady state besides solid, liquid, and gas states, known as plasma. From Langmuir's discovery, physicists realized that plasma constitutes more than 99% of the visible matter in the universe; stars, nebulae, and interstellar matter are all plasma though existing at a wide range of temperatures.

Since Langmuir's discovery, plasma has become a hot topic for researchers to explore. A number of theories about plasma behaviors and several plasma models have been developed to explore the fourth state of matter [30, 40]. The findings of these studies established the most important concepts of plasma physics, including the particle and fluid model, plasma damping, plasma decay, Debye sheath effect, and the collective behavior of plasma.

Just like the discussion of the light duality dilemma back in 1950, plasma can have fluid and particle characteristics together. After Einstein suggested the duality of light, various experiments started to verify the idea. Now, researchers all over the world are attempting to explore plasma's characteristics.

Since the invention of an ultrahigh-intensity laser achieved by chirped pulse amplification (CPA), lasers have become a source for producing plasma. Furthermore, since the first publication of particle acceleration from the laser-plasma interaction in 1995, the nonlinear and relativistic effects that ultrahigh-intensity lasers are capable of producing inside plasma have attracted researchers' attention. By the simple laser-plasma interactions, charged particles can be accelerated to several MeV energy. Between the accelerating potentials, an up to 10^{12} V/m electric field can be accumulated. This electric field lasts several femtoseconds to provide the force to accelerate particles coming out of the plasma.

A small and efficient particle accelerator was developed that provides a new perspective on particle and beam physics. From an overdense plasma, an efficient ion beam can be detected from the rear side of the targets, while from low density plasma, electrons are accelerated effectively. However, at this beginning stage, many more details need to be investigated, such as the optimum condition of acceleration or the mechanism of acceleration, in order to provide better particle sources for various applications.

The purpose of this thesis is to discover the mechanism and the optimum condition of proton acceleration from the ultrahigh-intensity laser and overdense plasma interaction in terms of the proton energy and flux. This topic is identified as being of importance to researchers in providing them more efficient proton acceleration from the laser-plasma interaction.

1.2 Laser-Plasma Research Regime

Laser-plasma research cannot start without the improvement of more and more powerful lasers. Since high power CO_2, KrF, and Nd:glass lasers were used to produce plasma for fusion experiments, researchers noticed that the characteristics of laser-produced plasma (LPP) depends on the laser intensity: the more powerful the laser is, the more nonlinear effects can be induced inside the plasma.

These nonlinear effects provide various interesting phenomena for researchers to explore. Namely, the mode-locking technique from the 1960's (see Fig. 1.1) and the chirped pulse amplification (CPA) [17] (see Fig. 1.2) in the 1990's have advanced the laser industry with much shorter pulse duration and much more energy in one pulse. These effects, together, provide orders of magnitude enhancement to laser pulse intensity.

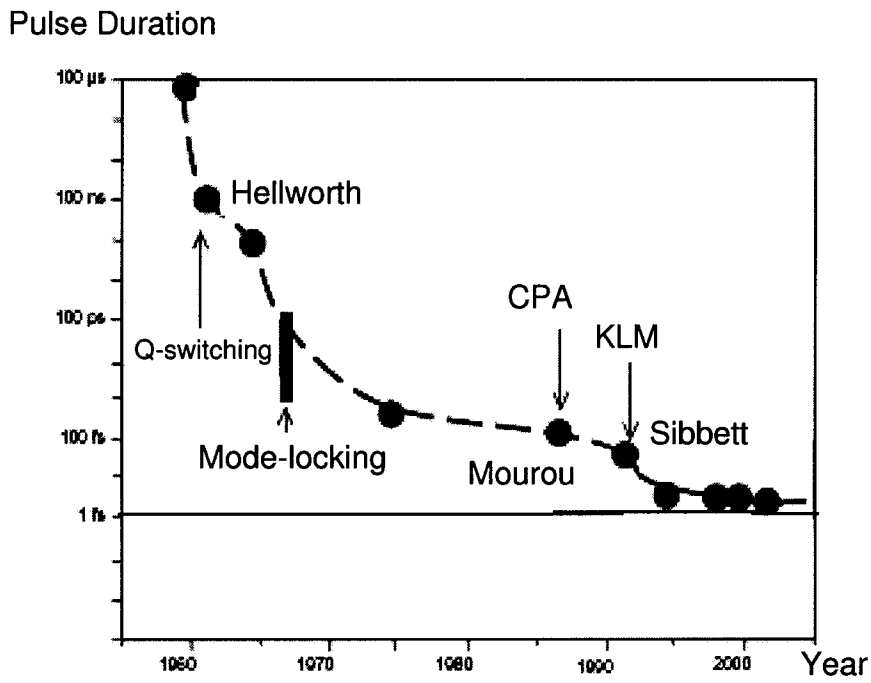

Figure 1.1: Evolution plot of laser pulse duration vs. time.

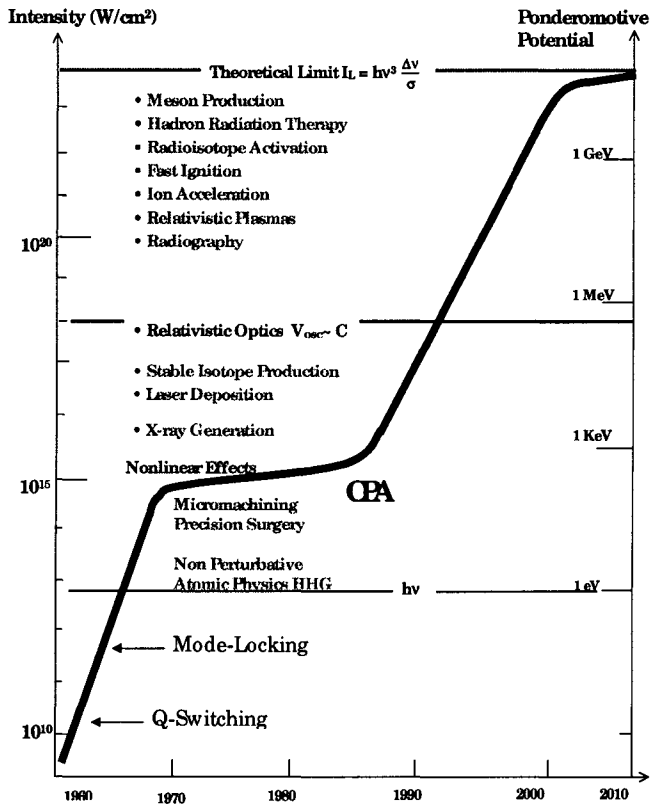

Figure 1.2: Evolution plot of laser intensity vs. time.

From Fig. 1.2, the CPA technique provides a tremendous improvement for the laser-plasma study. CPA made the intensity of a focused laser increase to 10^{18} W/cm^2. Such high intensity is sufficient to ionize the targets into plasma and quickly accelerate the particles into relativistic velocities, velocities comparable to the speed of light. This is called a relativistic plasma regime.

The University of Michigan's Center for Ultrafast Optical Science (CUOS) has been at the forefront of nonlinear interactions between lasers and materials. In 1961, the University of Michigan first observed the second harmonic generation phenomenon. Since then, researchers have been using stronger laser and field potentials

that are much larger than the electron binding energy in the atom to study nonlinear interactions. When the laser intensity became high enough, we immediately picked up the lead in, LPP physics research: CUOS was among the first few laboratories in the world to demonstrate the nonlinear optics in relativistic plasmas and laser wake field acceleration of electrons [60]. We also produced a MeV laser driven proton beam from a thin foil target [36]. Plasma-based laser accelerators have achieved the highest acceleration gradients of 100 MeV/mm for electrons and 10 GeV/mm for protons from solid targets, at about 10^{25} times higher than the earth's gravity, and yet higher gradients have been proposed and are under experimental investigation.

The interaction of electrons with both the oscillating magnetic and electric fields produced a number of nonlinear effects. When the electron velocity is comparable with the speed of light, the second term of the Lorentz force equation is no longer negligible (see Fig. 1.3). As a result, various nonlinear effects occur and more investigation is needed to understand laser-plasma interactions.

An extreme regime of focused laser intensity will be accessible soon with the development of the zettawatt-class (10^{18} W) laser systems, where protons will quiver relativistically in the laser field, elementary particles like pions will be produced, and the Compton γ^2 shift of the laser wavelength due to the co-moving accelerated electron beam will produce Gamma rays. This will allow more interesting nonlinear phenomena for high field plasma scientists to explore.

1.3 Thesis Outline

During the fours years in the CUOS of University of Michigan, three different laser-plasma interaction experiments and the theories behind them have been conducted and engaged. These three projects studied the mechanism and the method of

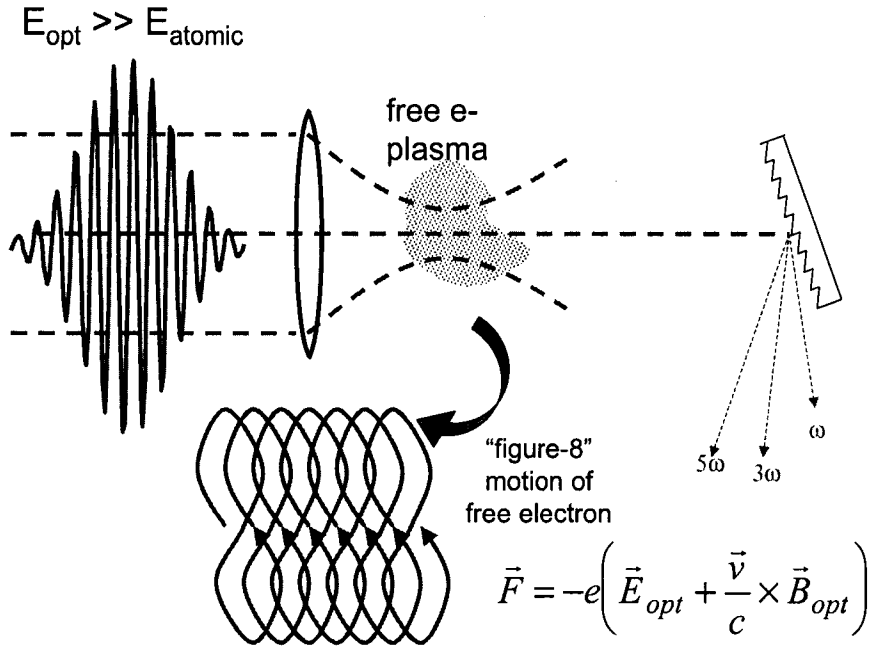

Figure 1.3: Schematic figure of ultrahigh-intensity laser interacting with plasma. The electrons are relativistic now and move in a figure 8 pattern [60].

controling proton acceleration from ultra-high intensity laser and solid target interactions. My thesis includes these three different projects as well as the background theory of the experiments.

An introduction of the T^3 (Table Top Terawatt) laser system is in Chapter III. The T^3 laser system is located in the University of Michigan's CUOS. The experiments reported in this thesis are all done with the T^3 laser system.

Chapter IV starts with electron angular distribution measurements, which provide a good understanding of the mechanism of proton acceleration. However, in the meantime, I learned from the electron distribution that we may also derive the surface magnetic field and see how the electrostatic field changes inside the targets.

Chapter V shows the proton beam images from long-scale-length laser-plasma interactions. Observation of these interactions indicates the effects of target material and target thickness on proton beam spatial profiles and proton maximum energy.

Chapter VI discusses the prepulse effects on proton acceleration. It shows the relationship between prepulse intensity and maximum proton energy.

Chapter VII shows some preliminary results about applications of the proton beam from ultra-high intensity and solid targets. These applications take the advantages of the compactness and low-cost of laser-driven proton acceleration to achieve their goals.

Chapter VIII concludes this thesis by summarizing the effects of electrons, target materials, target thickness and the laser condition on maximum proton energy.

CHAPTER II

Theory: Plasma Physics and Laser Accelerator

2.1 Plasma Physics

The fourth state of matter, plasma, is the main regime I will deal with when ultrahigh-intensity lasers interact with solid targets. This plasma is a gas of charged particles, which causes the gas to absorb more energy. One known characteristic of plasmas is the "shielding" effect. The shielding distance is called Debye length λ_{De}:

$$\lambda_{De} = \sqrt{\frac{\epsilon_0 k T_e}{n_e e^2}} \tag{2.1}$$

where ϵ_0 is the permittivity of free space, k is the Boltzman constant, T_e is the electron temperature, n_e is the electron number density, and e is the electron charge. For distances $r \gg$ the Debye length, the shielding cloud composed of the particles in the plasma effectively cancels all the outside forces.

For a classical plasma, a single particle motion is considered. Consider a slab of plasma of thickness L, where there are ions and electrons present and the ions have an infinite mass to make the ions immobile while the electrons can move freely through the ions. When an electric field is added, the electrons are pulled back and forth around the ions, creating a motion similar to simple harmonic motion with a

frequency w_e, called electron plasma frequency:

$$w_e = \sqrt{\frac{n_0 e^2}{\epsilon_0 m_e}} \tag{2.2}$$

Where n_0 is the electron density and m_e is the electron mass. By analogy with the electron plasma frequency, we define the ion plasma frequency w_i for a general ion species with density n_i and an ion charge Ze as

$$w_i = \sqrt{\frac{n_i Z^2 e^2}{\epsilon_0 m_i}} \tag{2.3}$$

Where m_i is the ion mass. But we can see from 2.3 that the ion plasma frequency is much smaller than the electron plasma frequency; therefore, considering the plasma as a fluid, we only need to consider the equations of motion for the electrons. Just like a usual classical wave, all the Maxwell equations, wave equation, and dispersion treatments are appropriate for electrons in plasmas.

Inside a relativistic plasma, nonlinear effects need to be taken into account. Lorentz factor γ is a factor used to determine the degree of relativistics for particles or waves.

$$\gamma = \frac{1}{\sqrt{1 - (\frac{v}{c})^2}} \tag{2.4}$$

Where the v is the velocity of the particles or waves, and c is the speed of light.

An important parameter for relativistic phenomena is the *normalized vector potential*, a_0.

$$a_0 = \frac{eE_0}{mwc} \tag{2.5}$$

Where E_0 is the electric field of the wave; m is the mass of particles; w is the frequency of the laser light.

a_0 provides information as to how strong the laser electric field is. We can now relate the γ and the a_0 by:

$$\gamma = \sqrt{1 + \frac{a_0^2}{2}} \tag{2.6}$$

or $a_0 = 0.85\lambda_0(um)\sqrt{I}(10^{18}W/cm^2)$. This high electric field wave induces nonlinear motion from the second term of the equation of motion, the $v \times B$ term; therefore, we can derive the ponderomotive force by plugging in the E and B relations twice to produce the formula:

$$f_{NL} = -\frac{1}{4}\frac{e^2}{mw^2}\nabla E_s^2 \tag{2.7}$$

A significant amount of density fluctuation occurs in the laser-plasma interaction zone because of coupling of the light wave and the electron-plasma waves. Furthermore, sizable ion density fluctuations can be produced in this interaction, due to the fact that an excited plasma wave interacts with the laser wave to generate changes in the electric field. Moreover, the gradient in the field gives rise to a ponderomotive force which can raise the ion density fluctuations [30]. This ponderomotive force and corresponding ponderomotive potential are the most important concepts derived from the nonlinear and relativistic plasma regime. They contribute to the relativistic plasma effects. For the refractive index changes, relativistic self-focusing, self-guiding, and self-phase modulation will be introduced. In an underdense plasma, this ponderomotive force can be high enough at a longitudinal direction to push electrons off-axis. This is also called ponderomotive self-focusing because the refractive index is higher at the axis.

Another important background element of plasma physics is its instability. No matter whether the plasma is treated by a single plane wave of finite amplitude (parametric instability) or by Vlasov fluid theory (two-stream instability), the plasma

in equilibrium is not necessarily in a stable state. In other words, even when the plasma is in equilibrium, we still can ask whether it is at a stable or unstable state. This is called parametric instability [40], and it includes parametric decay instability, stimulated Brillouin backscattering instability, and two-plasmon decay instability.

2.2 Laser Absorption and Heating

2.2.1 Collisionless Absorption

For a p-polarized light wave, the electric field has a component along the plasma density gradient. The oscillation of the field can generate fluctuations in the plasma, which causes the plasma to resonate. Therefore, the energy from the laser light wave can be transferred to the oscillation inside the electron plasma wave. This is called **resonance absorption**. Note that the oscillation in electron densities, which results in a charge density fluctuation at $\omega_{pe} = \omega$, can provide a different and changing wave number at the density gradient direction. After integrating the electric field inside the plasma density region, this can give an energy flux absorbed by the plasma, as follows [30].

$$
\begin{aligned}
I_{abs} &= \int_0^\infty \nu \frac{E_Z^2}{8\pi} dz \simeq \frac{wLE_d^2}{8} \\
E_d &= \frac{E_{FS}}{\sqrt{2\pi wL/c}} 2.3\tau e^{(-2\tau^3/3)} \\
\tau &= (\frac{wL}{c})^{1/3} \sin\theta
\end{aligned}
\tag{2.8}
$$

A recent publication also showed the agreement of the experimental measurements and the predicted scaling from resonance absorption [42].

2.2.2 Not-So-Resonant, Resonant Absorption

When an intense laser light wave has an oblique incident angle on a sharply bounded overdense plasma, a strong absorption can be accounted for by the electrons

that are dragged into the vacuum and sent back into the plasma with velocities that equal the electron oscillation velocity [6]. With an incident angle θ, the energy flux absorbed by the plasma is shown below.

$$I_{abs} = (\frac{\eta}{2\pi})\frac{v_{osc}E_0^2}{8\pi} \tag{2.9}$$

This mechanism is more efficient than the usual resonant absorption for $v_{osc}/w > L$, with the L being the density gradient length.

2.2.3 J×B Heating

J × B heating is a heating mechanism which originates from the oscillating component of ponderomotive force at normal incidence [31]. This indicates that, when the ultra-high-intensity laser is incident on the plasma, an electrostatic field driven by the ponderomotive force is established inside the plasma. This oscillating field has a strong spatial variation in the laser-plasma interface and is able to heat the electrons that interact nonadiabatically with it. With an incident laser intensity of 10^{18} W/cm^2 on a 100 n_c plasma, there is a total of 11% of the laser light being absorbed by initial-temperature 4 keV electrons [31].

2.2.4 Self-Modulated Laser Wake-Field Acceleration

A new mechanism supported by experimental results leads to efficient acceleration of electrons in plasma by two counterpropagating laser pulses. It is triggered by stochastic motion of electrons when the laser fields exceed some threshold amplitudes, as found in single-electron dynamics. In vacuum or tenuous plasma, electron acceleration in the case with two colliding laser pulses can be much more efficient than with one laser pulse only. In plasma at moderate densities, such as a few percent of the critical density, the amplitude of the Raman-backscattered wave is high enough to serve as the second counterpropagating pulse to trigger the electron

stochastic motion. As a result, even with one intense laser pulse only, electrons can be heated up to a temperature much higher than the corresponding laser ponderomotive potential [51, 52]. When an intense laser pulse interacts with a solid-density target, it is partially reflected, and the beating between the incident and reflected light in the underdense plasma region will create interference [43], which can modify the optical properties of the plasma, excite plasma waves and heat electrons [64].

2.2.5 Collisional Heating

The electrons in the plasma wave that absorbs the laser light energy will start damping. In particular, electron-ion collisions are one of these damping mechanisms. The coherent motion of oscillation of electrons in the laser electric field wave is transferred to thermal motion at the rate at which electron-ion collisions occur. We can calculate the damping rate by balancing the energy dissipation.

2.2.6 Collisionless Damping

An electrostatic wave can be damped, even without any collisions. This phenomenon is also called **Landau Damping**. When the velocity of electrons is near resonance, the electrons can exchange energy with the electron plasma wave, and the electrons can be accelerated or decelerated. We can calculate the changes in the energy of particles moving in a given field and then average these energy changes over a Maxwellian distribution (assuming the particles have Maxwellian distribution). After balancing the energy changes, we can obtain the damping rate from this collisionless process.

2.3 Ion Acceleration from Ultrahigh-Intensity-Laser and Solid Target Interaction

Many different phenomena take place in laser-plasma interactions. Fig. 2.1 shows at which regime each process needs to be considered in terms of plasma density and scale length [30].

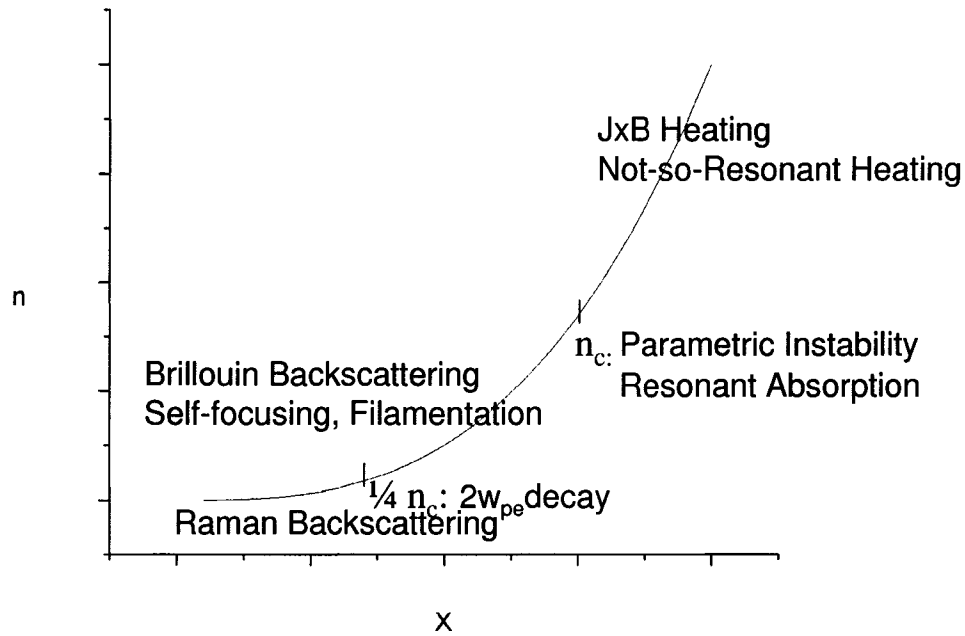

Figure 2.1: Schematic of density profile in plasma.

Working with ultra-high-intensity lasers needs to take into account all the nonlinear effects. This thesis mainly focuses on the "ultrahigh-intensity-laser" and "solid target" interactions because solid targets can provide energetic protons that are desired for the proton beam applications. Moreover, there are several special points that need to be considered for these overdense plasma interactions, which is discussed below.

2.3.1 Laser Intensity Contrast Ratio Effects

An ideal laser pulse has a huge signal-to-noise ratio; however, in current laboratory settings, such ideal clean-pulses are unachievable. A prepulse coming from an imperfect pulse compression or amplified spontaneous emission (ASE) can cause prepulses and pedestal preplasma.

In particular, the imperfection of pulse compression is very typical in a chirped pulse amplification (CPA) laser [55]. The bandwidth mismatch between the stretcher at the beginning of the laser chain and the compressor in the final stage of the laser chain is the main source of the prepulse, thus generating a low-density, preformed plasma that prevents sharp edge plasma formation produced by the main pulse.

Secondly, the ASE produced from the amplification process within the gain medium required in the regenerative amplifier (RA) and regular multipass amplifier can cause a prepulse pedestal. This ASE mainly comes from premature self-lasing in the nonlinear crystals. It not only will distract energy from the pumping laser so as to decrease the laser output, but it will interact with the target material before the arrival of the main pulse, thus decreasing the efficiency of the acceleration of particles. From theoretical calculations [34], assume a laser oscillator emits a series of pulses with power P_0 and with negligible noise power between pulses. Fluorescence from the amplifier's gain medium is emitted in all directions with random polarization. Only a small fraction of the fluorescence coincides with the injected pulses in the propagating direction. Part of the initial noise power p_0 (ASE) is amplified along the pulse.

The initial signal-to-noise ratio is defined as $R_0 = P_0/p_0$. Then after N round trips, the contrast ratio is $R_N = P_N/p_N$. The pulse power is, in absence of gain saturation, $P_N = G_a^{2N} P_0$, where G_a is the initial, single pass power gain on the line

center. The calculated noise power is:

$$p_N = \frac{p_0 G_a^{2(N+1)}}{(G_a^2 - 1)[1 + 2(N+1)g_a]^2} \tag{2.10}$$

where g_a is the round trip amplitude gain coefficient at the atomic line center. Thus, we can derive the contrast ratio after N round trips as:

$$R_N = R_0 \frac{G_a^2 - 1}{(G_a^2)[1 + 2(N+1)g_a]^{0.5}} \tag{2.11}$$

Also the p_0 is given by:

$$p_0 = \frac{\lambda_a^2 h\omega_a g_a \Delta w}{32\pi\sigma_a \tau_f \Delta\omega_h \sqrt{\pi ln2}} \tag{2.12}$$

The next step is to plug in experimental values associated with Ti:Sapphire crystals. These are as follows:

$\lambda_a = 1.053$ μm,

$h\omega_a = 1.186 \times 10^{-18}$ J,

$g_a \sim 0.2$,

$\Delta\omega/\Delta\omega_h = 1$,

stimulated emission cross section $\sigma_a = 3 \times 10^{-19}$ cm^2,

fluorescence lifetime $\tau_f = 3.2\mu$s,

which can give a value of $p_0 = 1.84 \times 10^{-5}$ W, and with an initial peak power $P_0 = 0.1$W, the expected contrast ratio $R_0 \simeq 5.43 \times 10^3$, and with a 60 round trips for the regenerative amplifier.

With these values, an expected contrast ratio from the RA about 10^5 can at least, theoretically, be obtained. From the calculation above, one can notice that the injection power also becomes an issue affecting the pulse intensity contrast. Obviously, when the injected seed pulse power is higher, the contrast ratio will be larger. This is

due to the fact that an injected seed pulse with high energy needs less cavity build-up time, thus reducing the number of round trips of the ASE that can be amplified.

In order to evaluate the contrast ratio, a pulse temporal intensity distribution trace was taken by a third-order autocorrelator. See Appendix A for details about the experimental setup. The trace outcome is shown in Fig. 2.2.

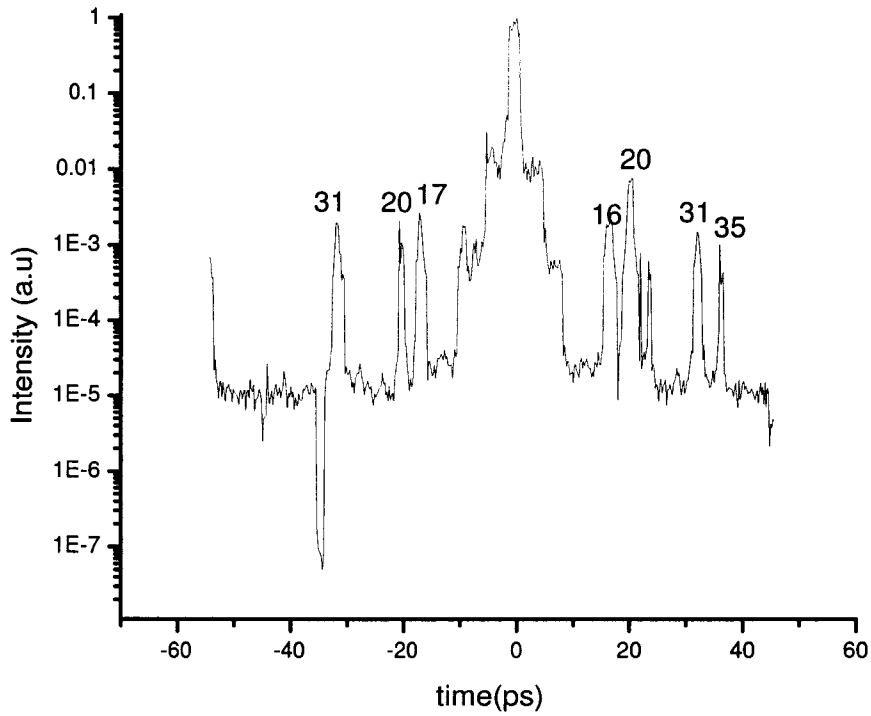

Figure 2.2: Third-order autocorrelator trace of T^3 laser, July 18, 2004.

The horizontal axis is scaled with time in picoseconds, and the vertical axis is scaled I/I_{max} in arbitrary units for Fig. 2.2. The maximum of the UV signal occurs when the fundamental and the second harmonic generation signal have the same optical length.

The setup has seven orders dynamic range. If one of the arms is blocked, the third harmonic signal disappears at the noise level that is seven orders of magnitude

smaller than the maximum. This is shown on the plot at about 35 picoseconds.

The main peak approximately shows a 500-femtosecond full width half maximum if I assume the shape of the pulse is Gaussian. This measurement is a little larger than expected. This discrepancy should come at the resolution of the long-range translational stage, which introduces the delay between the fundamental and the second harmonic generation signals.

The steps through which the stage travels are too large, so the process of fitting to a Gaussian distribution is not accurate enough because of an insufficient number of data points. This problem will be easily solved by replacing the present setup with a higher resolution stepping motor.

From Fig. 2.2, although I cannot identify exactly how long the pedestal would be, I can expect that the signal is decreasing toward the outer ends of the plot. The worst contrast for the pedestal would be five orders. This means that, when the laser main pulse is focused to an intensity of 10^{19} W/cm^2, the pedestal intensity can be as high as 10^{14} W/cm^2 at nanoseconds before the main pulse arrives.

In addition to the main pulse, there are several peaks around the main pulse. The positive time is the front side of the main pulse, and the negative side is the rear side of the main pulse. If prepulses exist, these prepulses must have arrived before the main pulse and caused the target heating, ionization, plasma formation, and the plasma expansion. This expanded plasma is called "preplasma." If other peaks appeared at the rear side of the main pulse, they would not cause too many problems; therefore, I will only discuss the prepulses in front of the main pulses. Fig. 2.2 shows that there are three pairs of symmetric pulses. These are mainly caused by the autocorrelator, such as the reflection from the neutral density filters, the doubling crystal, or the tripling crystal. These three pairs occur at 16, 20, and

31 picoseconds. I will disregard these artifacts from the autocorrelator. The pulse at 35 picoseconds, which is a 4 mm delay is a reflection from a BG-39 filter in the green arm only.

These data suggest that either the prepulse or the pedestal of the main pulse can introduce a more complicated process during the ultrahigh-intensity-laser and solid target interaction. When the laser pulse is incident on a solid target, the highest intensity part of the laser pulse is interacting with the preplasma at the plasma-critical surface instead of interacting with the sharp solid target surface.

Estimated preplasma length is a few microns for an intensity of 10^{14} W/cm^2 prepulse. Unfortunately, this makes the laser pulse interact with this underdense preplasma first, thus changing the solid target conditions. From a previous report [61], it was shown that nonionizing prepulses with intensities as low as $10^8 \sim 10^9$ W/cm^2 can substantially alter high intensity laser-solid interactions. The prepulse-heating and vaporization of the target can lead to a preformed plasma once the vapor is ionized by the rising edge of the high-intensity pulse. Therefore, it is important to gain a better understanding of ion acceleration processes in this regime.

2.3.2 Ion Acceleration and Absorption

Since the appearance of the short-pulse laser, laser-matter interaction has undergone a significant change. Matter suffers a huge gradient electric field in an ultrashort time period; this process not only involves linear and nonlinear optics, but also plasma physics and particle physics. With such a high-intensity electric field (10^{18} W/cm^2), the plasma becomes relativistic and a high-frequency oscillation electrostatic field component from the ponderomotive force is developed. The frequency of the ponderomotive force is $2\omega_0$; therefore, this means that electrons are accelerated into the plasma twice every cycle by this ponderomotive force [62].

This shows a "train" of high energy electrons that are separated by a distance of half of the laser wavelength. This process can heat the electrons up to about 1.1 MeV, which is 26% of the incident laser field energy. While the electrons are accelerated, the huge laser light pressure punches a physical hole on the overdense solid target. The light pressure is $p_L = 2I/c \simeq 6 \times 10^3$Mbar with 10^{19} W/cm^2 intensity. Further, by balancing the momentum flux of the mass flow with the light pressure, we obtain:

$$n_{pi} M u^2 = I/c \tag{2.13}$$

$$\frac{u}{c} = [\frac{n_{cr}}{2n_{pe}} \frac{Zm}{M} \frac{I\lambda_\mu^2}{1.37 \times 10^{18}}]^{1/2} \tag{2.14}$$

where n_{pi} and n_{pe} are the ion and electron plasma density, u is the ion velocity, M is the ion mass, and Z is the charge state.

From this equation, we can obtain ion velocity of about 0.025 times the speed of light. This means that this ponderomotive force can accelerate the ions to a very high energy (about 10^{-3} Mc^2) level with 10^{19} W/cm^2 intensity. As the hole forms, the electric field of the light wave begins to drive the plasma electrons on the sides of the hole. As expected, the absorption efficiency increases with $\omega_0 t = 600$, and the effective temperature of the electrons transporting toward the rear side of the target is about 1.6 MeV. This experiment indicates a 45% increase in the temperature of the electrons when hole boring occurred.

As well as being heated, the electrons flow outward from the target, thus this electrostatic field starts to drive the ions to the velocity shown in Eqn. 2.14. Detectors on the rear side of the target show the accelerated ions at the rear side of the target.

2.3.3 Proton Shock Acceleration

Recent publication [53] showed two proton acceleration regimes: (1) proton acceleration due to the ambipolar fields arising in the free expansion of the strongly

heated electrons at the front and rear of the target, and (2) proton acceleration in a collisionless, electrostatic shock formed at the front of the target. The formation of an electrostatic shock with a high Mach number M= $v_{shock}/c_s \approx 23$, where v_{shock} is the shock velocity, and c_s is the local sound speed, with a laminar structure. In addition, because of the intense heating of the background electrons by the incident laser, the effective sound speed is quite large; therefore c_s/c can exceed 0.1. This high velocity shock is responsible for the acceleration of the highest energy protons, with clear signatures in the proton spectrum and phase space [53], and the proton shock acceleration dominates at the rage of parameters.

2.3.4 Target Normal Sheath Acceleration (TNSA)

A prevalent mechanism for ion acceleration from solid targets was developed by Wilks *et al.* [63]. This ion acceleration mechanism (TNSA) is the result of a "cloud" of hot electrons, generated in the blow-off plasma created by the laser prepulse interacting with the target, which go through the target and ionize the proton layer on the back of the target. These protons are then pulled off the surface by this cloud of electrons and accelerated to tens of MeVs, in tens of μm.

One of the main ideas the TNSA mechanism expresses is that the source of the protons or ions is from the rear side of the target. Wilks shows a Particle-In-Cell (PIC) code simulation result that clearly indicates that the front of the target expands spherically as a plasma due to the interaction with the prepulse. The main laser pulse follows and hits this plasma and the critical surface, generating a large number of hot electrons (the electron cloud). Since the target is transparent to these energetic electrons, the cloud extends past the back of the target, whereupon it ionizes. Then it accelerates the proton layer on the back of the target.

A modified acceleration mechanism appeared recently [48]. It is called the " **Mod-**

ified TNSA Mechanism." Several experiment reports observed a front sheath of target acceleration. Thus, Sentoku investigated the ions' source topic again by performing PIC code simulations. His results exactly matched many other experiment results. In developing this modified TNSA, Setoku explored the effect of electron recirculation on the rear side sheath acceleration and found that the peak proton energy increases in inverse proportion to the target thickness. Furthermore, he showed that low-energy protons can come from the front side of the target plasma sheath; the higher-energy protons are from the rear side of the target plasma sheath. The derivation follows: to know the ions' acceleration time in the sweeping potential by calculating:

$$M\frac{dv_i(t)}{t} = \frac{E_i(x)}{dx} = ZeE_x(x) \tag{2.15}$$

where x is the direction of laser propagation and this model is a 1D model, assuming that the electrostatic field is constant at the average of $E_{x0}/2$ in the Debye length. Then, the ion energy as a function of x is given by:

$$E_i(x) = (\frac{ZeE_{x0}}{2}x) \tag{2.16}$$

The acceleration time τ_{sw} is calculated by integrating half the Debye length:

$$\tau_{sw} \simeq \sqrt{\frac{M}{Zm\gamma_{os}}}\frac{\lambda_D}{c} \simeq \sqrt{\frac{M}{Zm\gamma_{os}}}\tau \tag{2.17}$$

where τ is a laser oscillation period. With $\tau_L > \tau_{sw}$, we get:

$$\frac{u_{sw}}{c} = \sqrt{\frac{2\phi_s}{Mc^2}} = \sqrt{\frac{2m}{M}(1 + \frac{I\lambda^2}{1.37 \times 10^{18}})^{1/2} - 1} \tag{2.18}$$

This is the maximum velocity which the ions can reach, but if the laser pulse duration is shorter than the sweeping duration, the energy cannot transfer totally to the ions due to the disappearance of the sweeping potential. Moreover, after the laser pulse

irradiation is over, the ion velocity is reduced to $(\tau_L/\tau_{sw})u_{sw}$. For a 500 fs laser pulse, $u/c \sim 0.028$, the peak proton velocity is shifted up with the recession velocity u, and the final ion velocity from the front side sweeping acceleration is given by:

$$v_{max} \simeq u + 1.5u_{sw} \tag{2.19}$$

Thus, the protons can be accelerated. From this derivation, it shows that the key to accelerating protons is the electrons' motion because the sweeping potential and the ponderomotive potential are built up by the electrons.

Many researchers have tried to simulate the path of the electrons. The modified TNSA mechanism has another important perspective about the electrons' movement, which is the advantage of electron recirculation.

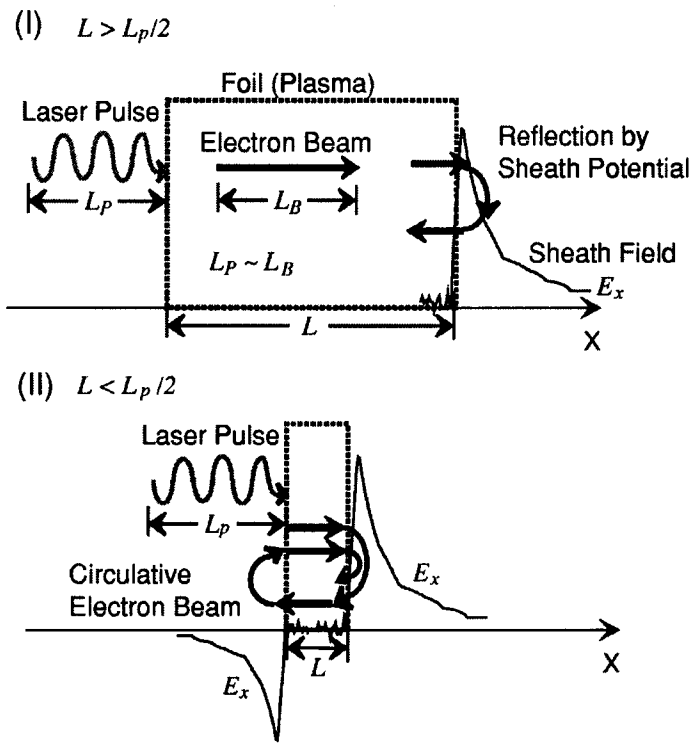

Figure 2.3: Schematic diagram of the relationship between electron recirculation and target thickness [48].

Fig. 2.3 illustrates that the hot electron bunch length is approximately the same as

the laser pulse length L_p, because the velocity of these hot electrons is approximately the velocity of light, c. The bunched electrons travel through the highly conductive target, like a metal or a plasma, without energy loss. They are then reflected at the target surface by a self-induced sheath field. When the target thickness, L, is greater than half of the pulse length, $L_p/2$, as seen in Fig. 2.3, the electrons overlap only locally at the target edge and there is no significant increase of hot electron density. When $L < L_p/2$, the electron recirculation can provide an increase of electron density. Note that the electron recirculation can only give a larger yield for electrons but not increase the electrons' energy, and the hot electrons do not lose energy inside the target; they circulate continuously until they transfer their energy to the protons. Moreover, the result shows that the more the electrons recirculate, the greater the number of electrons are driven, and overall, the more energy is stored in the electrons. When all the electrons transfer their energy to protons, the protons can gain more energy out of the higher electron recirculation. This suggests that a thinner target can provide more energetic protons.

Another 1D simulation [48], showed the difference between the front side and the rear side acceleration efficiency in terms of pulse duration, thus indicating that the rear side of the target has better efficiency of proton acceleration and gives higher maximum proton energy; however, there are still protons accelerated from the front side, although with lower energy. See Fig. 2.4.

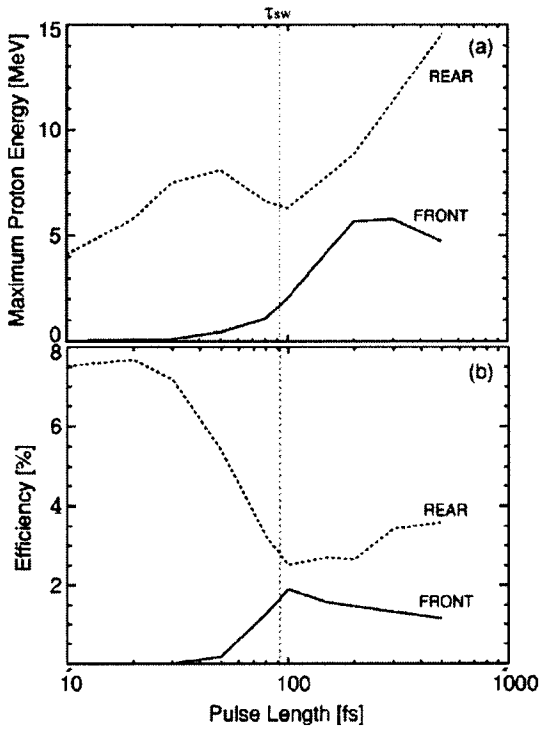

Figure 2.4: Front side vs. rear side acceleration [48].

CHAPTER III

Experimental Setup: Table-Top Terawatt Laser in Michigan

3.1 T^3 Laser System

The laser system used in this experiment was developed in the early 1990s. It is a 10 TW hybrid Ti:Sapph/Nd:Phosphate glass, CPA laser system with 400 fs pulse duration output. Four main components of T^3 laser are:(1) oscillator system, (2) regenerative amplifier system, (3) power amplifier system, and (4) pulse compressor.

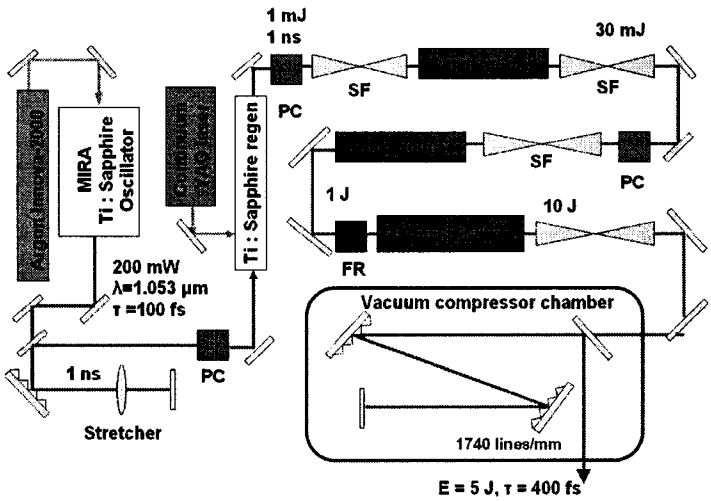

Figure 3.1: T^3 laser schematic plot, including the important parts of T^3 laser: an oscillator, a stretcher, a regenerative amplifier, three heads of amplifier, and a compressor.

The oscillator in T^3 is a commercial Mira-900 unit by Coherent that utilizes Kerr mode-locking to produce an 80 MHz, 2 nJ per pulse, 200 mW average power pulses

at 1.053 μm wavelength, 100 fs and 3mm diameter beam. The bandwidth of the oscillator output is about 7 nm. The oscillator is pumped by a commercial CW Argon ion multi-line (470-530 nm) laser (Innova 200 by Coherent) that emits a 10 W average power beam which pumps the Ti:Sapph crystal in the oscillator. The pulse train from the oscillator is sent to the stretcher, which can stretch out the laser pulse temporally by four passes of a single 1740 lines/inch grating into about a 1 ns pulse duration.

Afterwards, the beam is reduced in repetition rate, with a Pockel cell, down to 10 Hz before it enters the second component of the laser system, the regenerative amplifier (RA). The active medium in the RA is a Ti:Sapph crystal that is pumped by a commercial SureLight unit (by Continuum) through two arms that deliver about 30 mJ each in an 8 ns pulse at $2w_0$. The seed pulse from the oscillator gets amplified in the RA up to a 1 mJ level before it enters the third component of the system.

In the amplification chain, the pulse is first spatially cleaned by an air spatial filter, where a diffraction limited aperture at the center of the filter preserves the central disk in the Airy pattern beam profile. The spatial filtering takes place before the beam enters the first 16 mm diameter Nd:Glass rod amplifier.

These three heads in the amplification chain are water cooled and flash-lamp pumped. When the pulse exits the first head, the energy of the pulse will have been amplified to a maximum of tens of millijoules. A hard aperture is set up after the first head that defines the size of the beam at the output of the amplification chain. The pulse then enters another (vacuum) spatial filter that preserves the TM_{00} mode and relays images of the pulse with a minor 10% waist increase. Just before entering the second head, the pulse passes through a Pockel cell. This prevents the pulse from reflecting back to the system and helps reduce the Amplified Spontaneous Emission

(ASE) from the rods.

The pulse then enters the second head and gets amplified up to a maximum of about 1 J. Another vacuum spatial filter relays images and magnifies the beam size to three times of the incident beam. After that, the pulse passes through a half-wave plate and an active Faraday rotator sandwiched between two crossed polarizers. The Faraday rotator is a quarter-wave retarder, which means it prevents the pulse from reflecting from downstream. If reflection occurred, it would not be destructive because Faraday rotator would make the beam having the wrong polarization state, which would prevent the beam from propagating back into the amplification chain.

At this position, the pulse is ready to enter the last amplification stage in the third head, which is 45 mm in diameter. When the pulse exits the third head, it will have been amplified to a maximum of several Joules, and then the last vacuum spatial filter will relay the image of the beam again and increase its size. By then, the beam diameter will have reached its maximum beam size of 50 mm, and enters the compressor. Finally, the beam enters a two-pass grating compressor (1200 grooves/mm), where it is compressed to a pulse duration of about 400 fs, with about 60% efficiency.

The pulse contrast at the output is about 10^5 (see the details in Appendix A and Chapter II). This is a very important parameter for the interaction of high power lasers with the target. This contrast is considered adequate for experiments, as the pedestal of the pulse at I = $10^{-5} \times 10^{19}$ W/cm^2 = 10^{14} W/cm^2 will not induce too many pre-ionized electrons at the nanosecond pulse level. Because from the calculation of the preplasma scale length: $l = c_s \times t; c_s \sim \sqrt{\frac{T_e}{m_i}}$, where l is the preplasma length, c_s is the sound speed, t is the plasma expansion time, T_e is the electron temperature, and the m_i is the ion mass, the preplasma is about 5 μm, which

is small. The compressor and the subsequent laser system is kept under vacuum to prevent the laser beam from breaking up in air. To provide enough time for amplifier rod heat dissipation, 7 minutes are required between each shot.

3.2 Energy Measurement

The energy carried by the output pulse in front of the compressor is measured by a caloriemeter (Model 380401 by Scientech). The maximum output of T^3 laser is 6.5J (See Fig. 3.2).

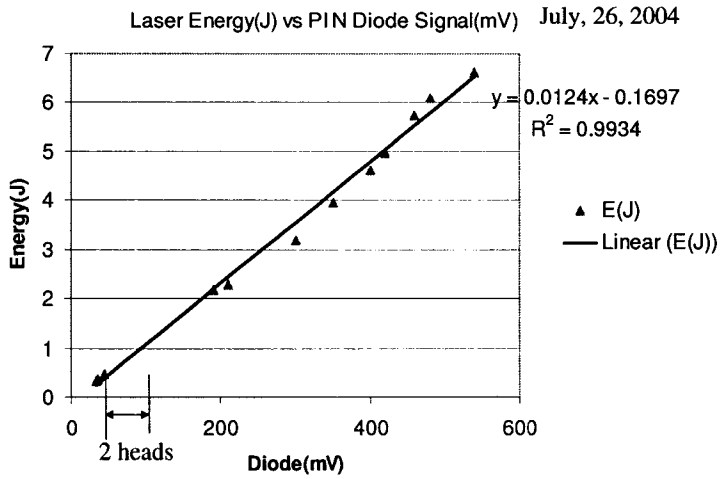

Figure 3.2: Energy calibration plot.

During the experiment, the energy of the shot can be measured simultaneously if a referenced diode is installed. Installed in the laser system, it detects the leakage from the laser pulse in front of the compressor. In this case, the real time pulse energy level can be measured by the caloriemeter after the diode voltage output has been calibrated. Fig. 3.2 shows the calibration data that predicts the laser pulse energy.

3.3 Experimental Chamber Setup

The experimental chamber setup schematic plot is shown in Fig. 3.3. This is a top view of the chamber. The laser pulse after the compressor has an intensity

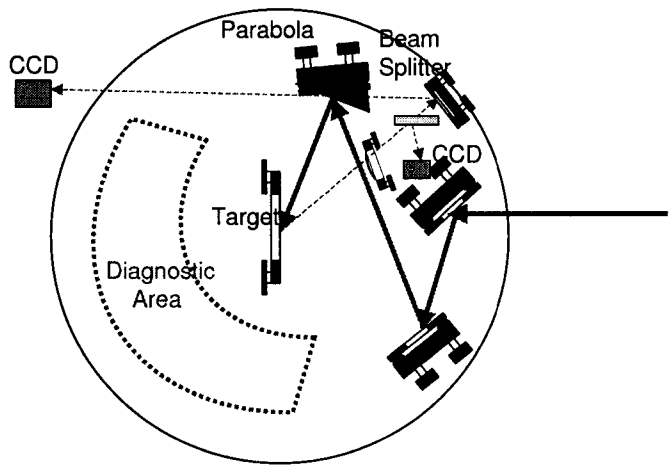

Figure 3.3: Experimental chamber schematic plot.

10^{11}W/cm^2, which is enough to interact with the air and produce some nonlinear phenomena; therefore, with a full power beam, a low vacuum must be created in order for the pulses to propagate. To reduce the nonlinear effect on the beam profile, the vacuum level should be less than 100 mtorr. Inside the experimental chamber, vacuum-compatible optical components should be used.

In the figure, the arrow from the right pointing to the left is the laser pulse propagation direction. The laser beam is 2 inches in diameter. When the laser enters the experimental chamber, usually, a 33-degree-off-axis f/3.3 dielectric parabola is used. For different purposes, a shorter focal length parabola, 15-degree-off-axis f/1.5, will be used as well.

Both the parabola mirrors are coated with both 527 nm and 1 μm wavelength light. The target plate is an optically flat 500 μm thick silicon wafer with 3 mm diameter

holes etched through. When the thin film target is glued to the flat surface, the foil will be exposed in the etching-through holes.

Inside the chamber, an 8-bit CCD camera is installed to look directly at the target plate for the alignment of the holes. This is called the low-magnification system. It provides an overview of the target plate when the experimental chamber is under vacuum.

A P-I-N diode, which is a good monitor of the x-ray emission, is installed in the direction of plasma expansion. X-ray signals are always a good indicator of the alignment of experimental setup. The x-ray signal is larger when the target plate is put at the focal position of the parabolic mirror.

Outside the chamber, there is another 8-bit CCD camera that can take an image of the reflection of the laser focal spot on the thin foil target. It is called a high-magnification system. About three times magnification is achieved by putting in a lens; this lens collects the scattering from the thin film target at target normal direction. By using the high magnification system and then fine tuning of the parabolic mirror, the target plate can be moved to the focal point during the experiment.

3.4 Focal SpotSize Measurement

Fine adjustments of the parabolic mirror are required to optimize the size and shape of the target spot. The smaller the spot is, the higher the peak intensity of the interaction. This step ensured that the spatial profile of the target spot is uniformly flat. To facilitate the adjustment, a 60 times magnification objective lens is installed into the setup before the chamber is pumped down to a vacuum. Fig. 3.4 shows the experimental setup.

Fig. 3.5 shows a typical focal spot measurement lineout. It shows that the Full

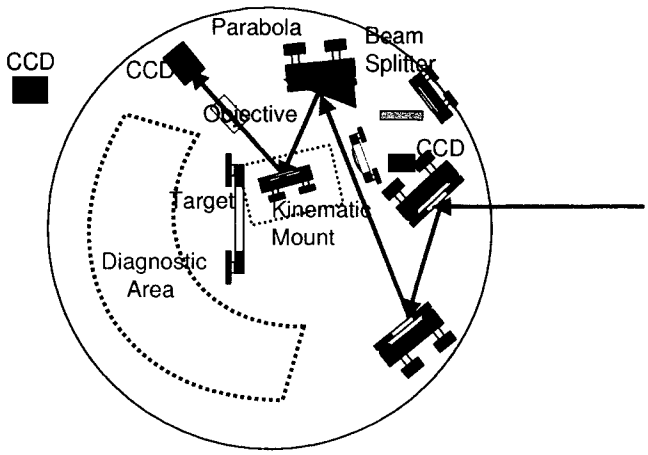

Figure 3.4: Experimental setup for measuring the focal spot at the target surface.

Width Half Maximum (FWHM) spot diameter is about 6.8 μm. The energy coverage within the FWHM diameter area is, at most, 40% of the incident beam's energy.

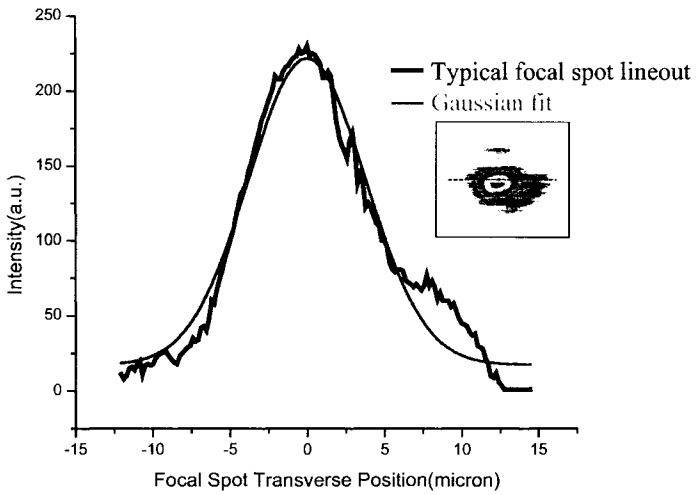

Figure 3.5: Focal spot analysis, the spot lineout, and the image of the spot.

CHAPTER IV

Experiment: Electron Generation from Laser-Solid Interaction

The physics of ultraintense-laser and solid-target interactions has been explored for years. For example, a collimated beam of fast protons was reported from ultrahigh-intensity-laser and solid-target interactions [10, 25, 36, 54]. A target normal sheath acceleration mechanism was established [63]. All of these experiments indicate that electrons are the driving force of the proton acceleration process.

However, a thorough analysis of the angles and energies of laser-generated electron distribution has not yet been developed. Some important applications rely on the generation of fast electrons from the laser-solid interactions, such as fast ignition of fusion reaction [56], ultrafast radiation generation [58], and material science research. Therefore, fast electrons generated in the interaction of ultrashort intense laser pulses with solid targets play an essential role in laser plasma interactions.

4.1 Experimental Setup

Electrons have small mass and they can easily respond to electric and magnetic fields in laser-produced plasma. Previous theoretical publications show that, while electrons are transporting inside the solid in a collisional plasma [32, 14], magnetic instabilities (Weibel instability) produces a filamentation phenomenon of electron

beams through the rear side of the target [21, 26, 49]. On the other hand, the electrostatic potential built up by the charge separation during the interaction has a femtosecond time scale, which is still a challenge for direct measurement. The difficulties come from the fast-evolving particle ionization of the medium; therefore, making a direct measurement of these changes in such a short time scale difficult. In [57, 58], the indirect measurements of the electrostatic fields and the magnetic fields are obtained by observing the changes of the polarization of the harmonic generated from the interaction and the x-ray fluorescence or optical probing; however, these methods require complicated setups and introduce large errors into the measurements.

In this chapter, a thorough electron angular distribution from the ultrahigh-intensity-laser and solid target interactions is investigated. The experimental angular distribution results show an explicit correlation with the particle-in-cell (PIC) code results.

A clear electron beam is observed at the rear side of the target; however, this electron beam did not follow that of the ions, which is in a direction perpendicular to the solid target plate, nor did it follow the laser on-axis direction. The dependence of the deflection angle is then derived according to our measurements.

In addition, another clear tendency is for the electron trajectory to flow along the tangential direction of the target plate. The analysis of the electron image shows that electrons are pushed from the laser-solid interaction point toward lateral extensions along the target surface. Moreover, from the electron ejection angle and the energy of the electrons, one can derive the electrostatic field changes in laser-plasma interaction and the magnetic field generated from the surface currents at the front side of the solid target [38, 59]. The electron beam, which flows close to laser

on-axis direction, and the electrons ejecting along the target tangential direction have not yet been reported. This is the first report to use the electron angular distribution to measure the electrostatic potential changes and the magnetic field generated from the interactions.

The laser beam is p-polarized and is focused by an f/3 parabolic mirror onto thin aluminum foil targets (13μm) positioned at 35 degrees to the axis of laser incident propagation. The peak intensity on the target is 1×10^{19} W/cm^2 at 7 μm FWHM focal spot size. Around the target plate, a half cylinder of an equal distance of 5 cm is aligned to wrap the rear side of the target at the laser incident plane.

Radiochromic films (RCF) and x-ray radiography film are the detectors for electrons. They covered the cylinder holder separately and faced the laser focal spot at the target to be exposed by the dosage generated from the laser-plasma interaction. See Fig. 4.1.

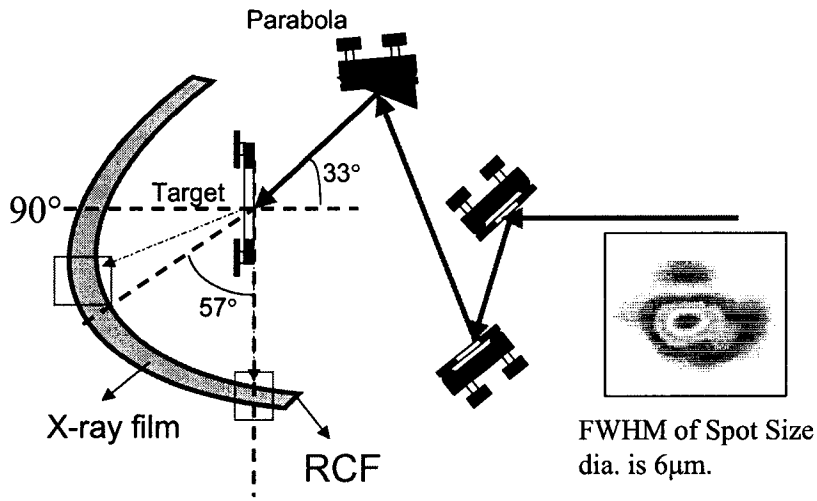

Figure 4.1: Experimental setup for electron observation by the films.

The x-ray film, Extended Dose Range film (EDR2) from Kodak film company, requires high exposures, 25~400 cGy [20]. The RCF used here is the MD-55, which is a thin film dosimeter that develops a blue color that is roughly proportional to

the absorbed dose when it is irradiated with ionizing radiation. The RCF needs no development procedure; it is based on polydiacetylene and has been introduced for medical applications, known as GafChromic MD-55.

The film consists of a thin microcrystalline monomeric dispersion coated on a flexible polyester film base. The film is translucent before irradiation. It turns progressively blue upon exposure to radiation. The radiochromic radiation chemical reaction is a relatively slow, first-order solid-state topochemical polymerization of the film. When the coated layer encounters radiation, the homogeneous planar polyconjugation along the carbon-chain shows a dark blue image. This gives a quick and clear idea of where the electron beam is.

4.2 Observation of electrons

Inserting aluminum step filters or a magnet spectrometer in front of the radiographic films provides an electron energy measurement. From the dosage images on the film, the relative flux information can be determined; from the calibration curves [20, 65], the absolute flux information can be calculated, as well. Moreover, these film measurements have the advantage of providing a spatial distribution. Based on the measurements described above, a direct and thorough electron angular distribution can be obtained by this method.

Fig. 4.2(a) shows a scanned image of the x-ray film from a typical shot at I=1×10^{19} W/cm^2; Fig. 4.2(b) shows the lineout of the real image picture in Fig. 4.2(a). Toward the left hand side of the film is the tangential direction of the target plate. As seen in the picture, there are two lobes of electron signals. The center position of these lobes corresponds to the tangent of the target plate; the spacing in between is the shadow of the target holder, which we can ignore. Toward the right hand side of the

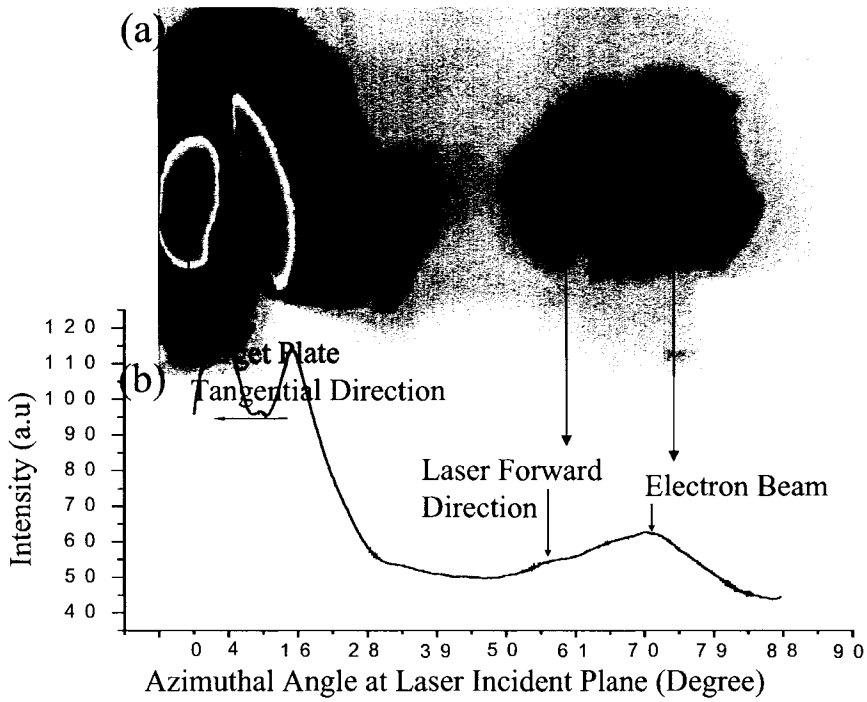

Figure 4.2: (a): A false color real image of the x-ray film which covers half of the circle of the laser incident plane at the rear side of the target shown in Fig. 4.1. (b): The lineout of the (a) image with labeled correspondent directions.

film is the normal direction of the target plate.

Two, clear, electron signals deposited on the film are worth noticing: one is in the direction of the tangent line of the target plate and the other is a smaller signal of electrons flowing close to the laser forward direction. This signal is more like a beam distribution compared to the broader distribution at the target plane.

4.2.1 Tangential Electron Analysis

Let's discuss electrons along the tangential direction first, which have not been reported in publications. In the target tangential direction, the electron energy spectrum was measured by aluminum step filters. Fig. 4.3 is the scanned image of the electron signal at the tangential direction. The electron temperature is 475 keV. Also at the target tangential direction, but outside the laser incident plane, x-ray film

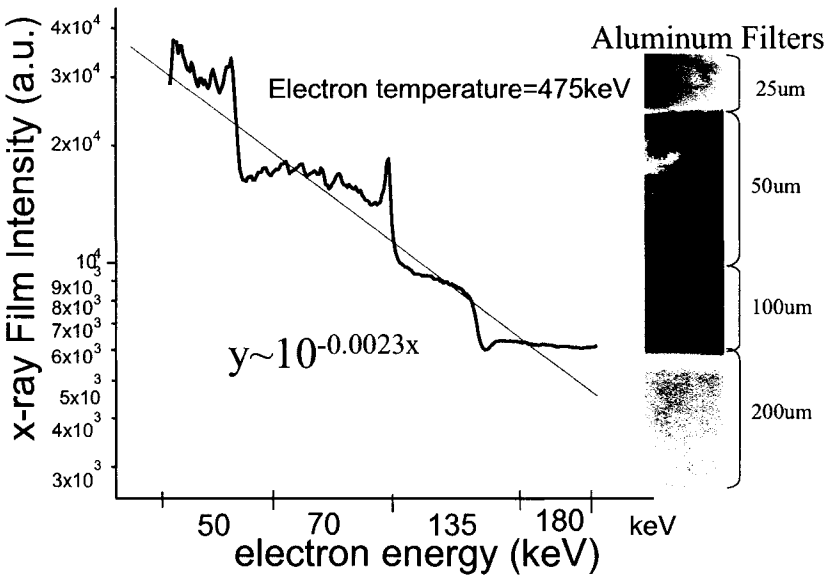

Figure 4.3: A x-ray film false color real image of the electron signals at tangential direction of the target plate with step filters (right) and its lineout (left).

detectors were installed on top of the target plate to measure the electron dosage; however, no significant electron signals were observed. This absence of electron signals shows the electrons are constrained within the laser incident plane.

Previous publications have studied the electron lateral extension distribution from solid targets [15, 17]; nonetheless, they observed a uniformly distributed circle of electrons around the laser plasma interaction point. This paper is the first to observe a nonsymmetric lateral distribution of electrons generated from the solid target which, instead of forming a circle, only flows along the laser incident plane. This nonsymmetric structure might suggest that the incident laser field momentum plays an important role in the lateral electron generation.

The electrons may be generated from a sharp laser-plasma interface with a nonadiabatic heating process driven by the ponderomotive force [62] at the front side of the target plate. As a result, the electrons will try to leave the heated region. In an one-dimensional symmetric case, the electrostatic field arising from the breakdown

of exact neutrality will return the electrons; however, in an asymmetric response case, the electrons will not return from the same path, although they will still flow backward to quasi-neutralize the original expansion. An electron current is formed and this net circulating, which is called surface current, will induce a magnetic field $\mathbf{B}$[22, 23]. After combining Faraday's and Ohm's law with the electron temperature gradient, electron density gradient, radiation pressure, and ponderomotive potential as driving terms, a magnetic field will be derived if the electron density gradient and the electron temperature are not parallel. Note that for the relativistic laser regime, the ponderomotive potential provides the largest contribution to the magnetic field. On the other hand, if the radiation pressure and the ponderomotive potential are not uniform in the transverse direction, this discrepancy also can serve as a driving force of the surface current. In [50], the experimental results and their corresponding theoretical predictions indicate that the quasisteady magnetic field induced by the high-energy currents can collimate the energetic electrons along the specular direction and pinch the electron stream. These results suggest that the magnetic field generated from accelerating the electron jet into the overdense plasma by the ponderomotive force is the key to affecting the trajectory of the electrons in the ultrahigh-intensity laser and plasma interactions.

Concentrating on the front side electron generation, which ponderomotive force has effects on, the overdense plasma is ionized by the incident ultrahigh-intensity laser, and the small-massed electrons are moved by the fields generated from the interaction.

From many previous publications [29, 50], a collimated electron jet has been observed. Assuming these electrons have a uniform momentum profile at jet transverse direction, they are injected into the solid target with momentum $(p_x, p_z)_{z=0} =$

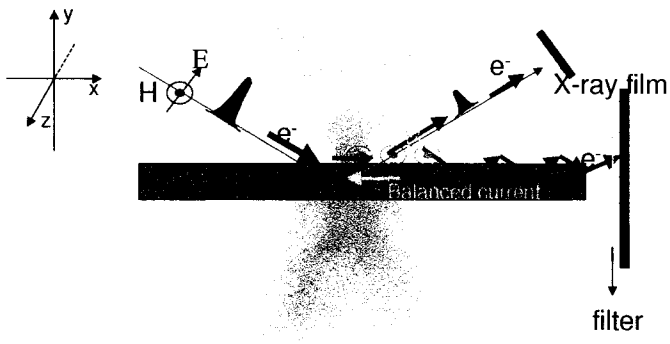

Figure 4.4: Movement of electrons at a tangential direction to the solid target. The green solid arrows show the electron trajectory. Electrons are first being reflected by the ponderomotive force toward the laser spectral direction, self-generated surface magnetic field, bent by the magnetic field and then pushed back by the space charge effect from the vacuum.

$(p_0 \sin\theta, p_o \cos\theta)$ with laser incident angle θ, where z is the target normal direction and x is the target tangential direction. This surface current will induce return current inside the target material and these two currents will form a loop to induce a magnetic field $B_y = \frac{\partial A(z)}{\partial z}$ at positive y direction. With canonical momentum conservation on the magnetic field effects, one can easily derive the charge and surface electron density with the injected electron momentum $p_0 \leq \frac{A(z_{ref})-A(0)}{1-\sin\theta}$ and reflected at $z = z_{ref}(p_0)$ by the induced magnetic field [38]. The electrostatic potential formed by these fields and the magnetic field then can be derived analytically with known boundary conditions.

The schematic figure (Fig. 4.4) shows the movement of electrons at a tangential direction to the solid target.

A 2D-PIC code simulation result of the surface magnetic field is shown in Fig. 4.5. These surface electrons can generate a surface magnetic field and, in turn, can bend other surface electrons. When these electrons flow away from the target (after having been bent by the magnetic field), the negative space charge effect pushes them

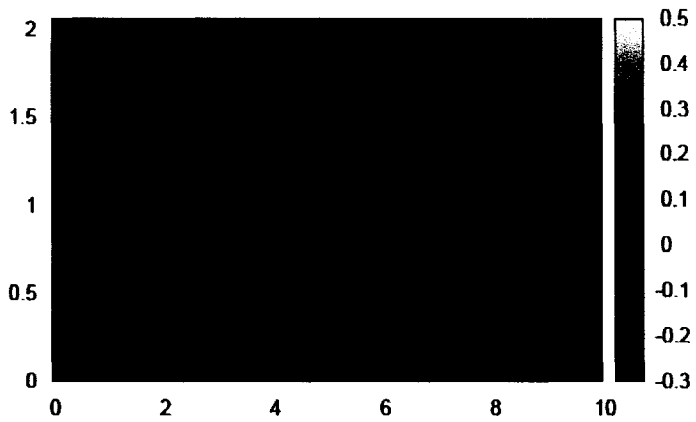

Figure 4.5: The simulation result of the magnetic field at the front of the solid target. The target density is ten times critical density, with a 2 micron width and an initial temperature of 500 eV. Laser condition: a_0=1; spot size is 1 micron; pulse duration is 25 fs. This plot is adapted from [38] by permission.

back toward the target. However, again, the induced magnetic field pushes the electrons away from the target plate. These electrons flow away from the laser-target interaction point and are constrained to the surface of the target. As shown in the simulation, the positive feedback mechanism zone can extend to a millimeter scale in the vacuum. Our x-ray film detectors are 5 cm away from the laser-plasma interaction point; however, after those electrons leave the active magnetic field, they still keep their momentum in the vacuum and deposited on the film detectors. Therefore, the electron trajectory spread causes a wider distribution of electrons on the image. The 2D-PIC code simulation (Fig. 4.6) verifies the observation of the electron signals at the tangential direction to the target plate. The surface magnetic field, **B**, has an estimated magnitude of 30 megagauss. This tangential direction electron signal is good evidence of the existence of the surface magnetic field. On the other hand, the electron observation at the target tangential direction mechanism depends on the magnitude of the magnetic field generated at the front surface, but the the target material, and the laser incident angle are also the factors to affect the mag-

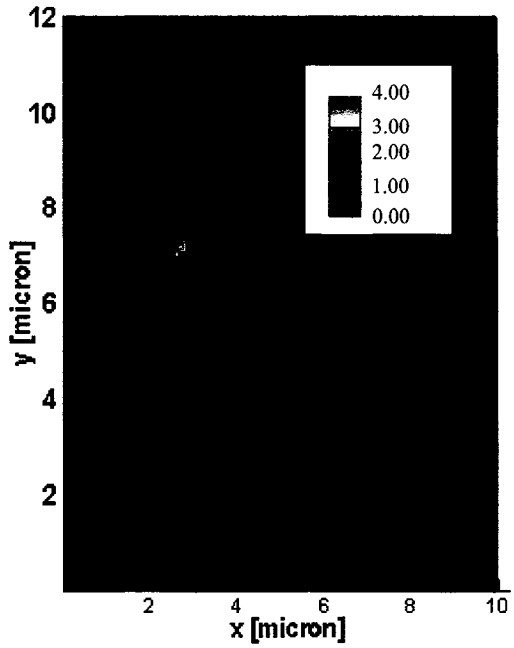

Figure 4.6: Electron density at the front of the solid target after the interaction. This plot shows the lateral direction spread of electrons. It is adapted from [38] by permission.

netic field generation. Therefore, more experiments can be designed to verify this surface magnetic field mechanism, and also observe the corresponded electron energy changes.

4.2.2 Electrons at Close to Laser On-Axis Direction Analysis

For the electron beam image observed close to the laser on-axis direction (see Fig. 4.7, Fig. 4.2), we found that there were a large number of high-energy electrons with a the direction θ in respect to the target normal direction. The laser incident angle with respect to the normal line of the solid target is α. We modeled the target plate with an electrostatic field throughout its thickness; therefore, the Hamiltonian of the electrons produced by the ultrahigh-intensity laser with the target is $H = \sqrt{1+(\mathbf{P}+\mathbf{A(x,y,t)})^2} - \Phi(x,t)$, where $\mathbf{P}$ is the canonical momentum [59], $\mathbf{A(x,y,t)}$ is the vector potential of the laser field and $\Phi(x,t)$ is the scalar potential with respect

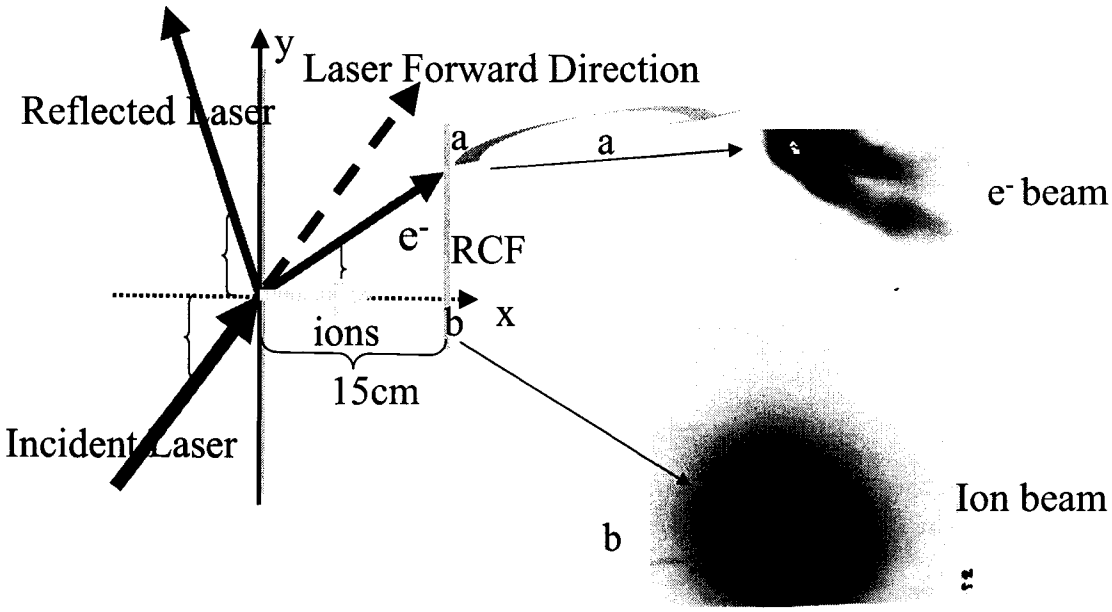

Figure 4.7: A schematic figure of the laser-target interaction and the corresponding measurement of the electron image.

to the electrostatic field.

Assume that electron energy changes in a time scale much shorter than the scalar potential, and H, Hamiltonian, is an adiabatic invariant of motion. Define $\tan(\theta) = \frac{p_y}{p_x}$ and $\gamma = \sqrt{1+p_x^2+p_y^2}$. With use of the adiabatic H, we can get:

$$\tan(\theta) = \pm[\frac{2(\gamma-1)(1+\delta\Phi)-\delta\Phi^2}{(\gamma-1-\delta\Phi)^2}(\sin^{-2}(\alpha)) + \tan^{-2}(\alpha)]^{-1/2} \tag{4.1}$$

where $\delta\Phi = \Phi(x,t) - \Phi_0$

This equation shows that the angle θ only depends on the electron energy, the laser incident angle, and the changes of the electrostatic potential affecting the electrons. These electrons first gain energy directly from the laser electric field. After the reflection of the laser pulse, the electrons are influenced by the induced electrostatic fields.

The 1D3V PIC code simulation (see Fig. 4.8) shows the angular dependence of the electrons' energy. For 500keV electron energy, it predicts that the deflection angle

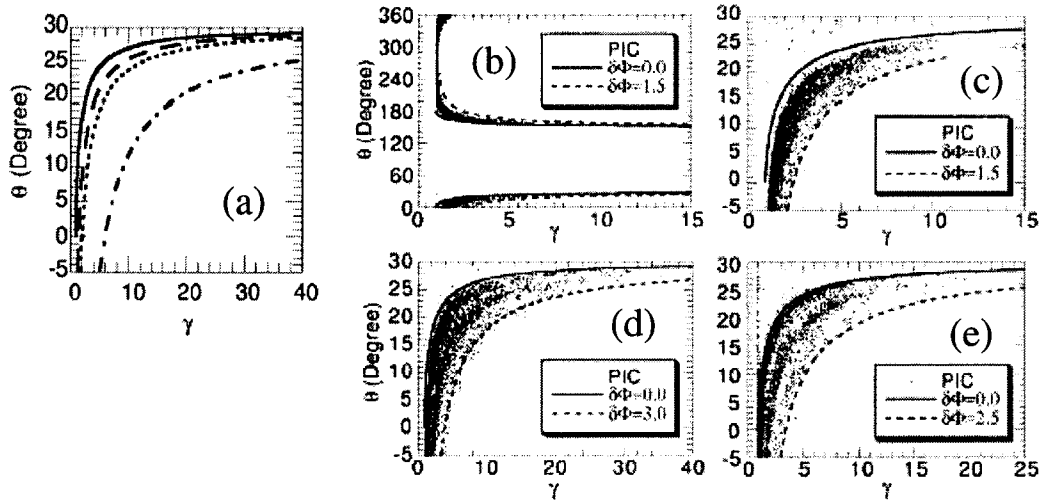

Figure 4.8: (a) shows the angular directions of electrons function of particle energy at various electrostatic potential levels when α=30 degree and the solid line is for $\delta\phi$ equals from 0, 0.5, 1 to 5 for different dashed line. (b)-(d) show the angular directions of electrons after the interaction of a laser pulse with solid targets(a_0=3, α=30 degree, t=50τ) with different scale length from 0, 0.3, and 3 times of laser wavelength. Other than (b)-(d), the laser is p-polarized, (e) shows the same simulation result with s-polarization laser pulse. This plot is adapted from [59] by permission.

θ is 18.8 degrees for 1 μm laser light at an intensity of $1 \times 10^{19} W/cm^2$ with 32 % electrostatic field potential changes. See Fig. 4.9.

Fig. 4.10 shows a beam image from a typical shot of the RCF film. The transverse divergence of the 7.30 cm-mrad beam centers at θ = 18.4 degrees away from the target normal direction with 500 keV energy. Our laser is at a 1 μm wavelength with 1×10^{19} W/cm^2 peak intensity at the focal spot. This angle agrees with the simulation result with the electrostatic field potential of 0.5 mc^2/e, providing good evidence that the angle θ only depends on the electron energy, the laser incident angle, and the changes of the electrostatic potential that the electrons experienced. This further suggests that this is a very simple and convenient method for measuring the changes of the electrostatic potential, which is the main field to accelerate protons from solid targets. There was no report on the direct measurements of these potential changes,

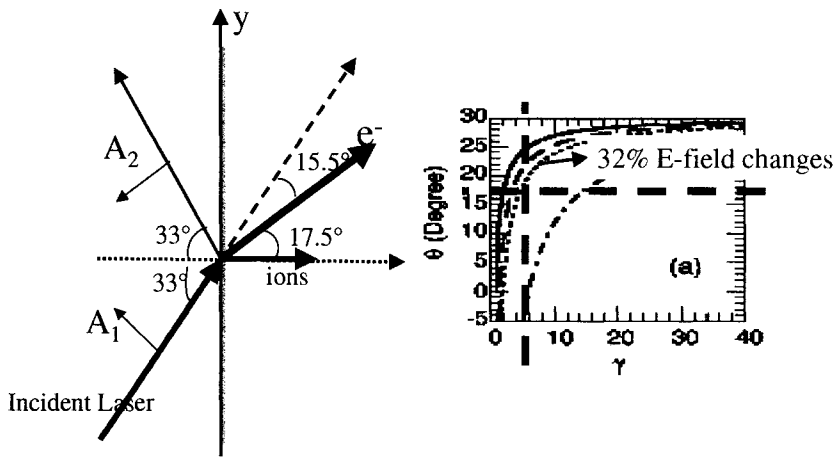

Figure 4.9: Schematic figure to show the agreement of the experimental measurement and the PIC simulation result. A 32 % electrostatic field potential changes is predicted.

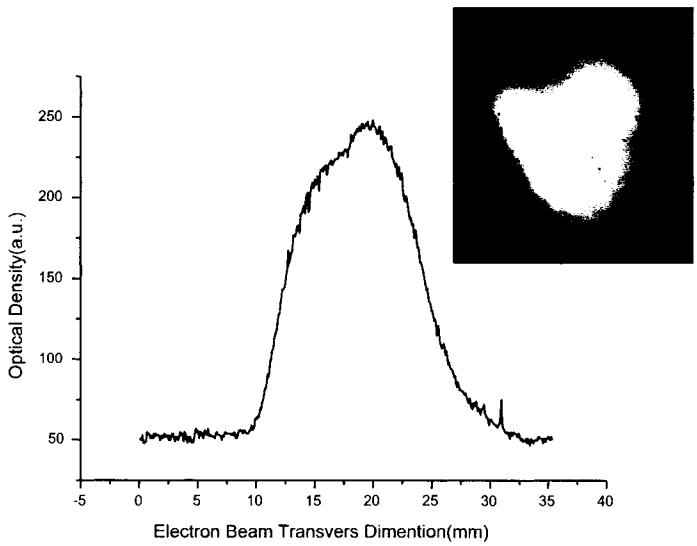

Figure 4.10: A false color image of RCF of the electron signals at rear side of target plate close to the laser incident direction.

and the electron angular distribution that we suggested provides a convenient method of achieving this goal.

4.3 Summary

The experimental study of the angular distribution of fast electrons provides a beneficial measurement to obtain the potential electric changes and the magnetic field generated from the ultrahigh-laser and solid target interactions. A clear electron beam was observed at the rear of the target; however, this electron beam did not follow the direction of the ions, which move in a direction perpendicular to the solid target plate, nor did it follow the laser on-axis direction. The deflection angle generated from the interaction was then derived. In addition, another clear tendency for the electron trajectory to flow along the tangential direction of the target plate was observed. Analysis of the electron image shows that electrons are pushed from the laser-solid interaction point along the target surface. These electron distributions can indicate electrostatic field changes inside the target plate and the magnetic field that are induced from laser-plasma interactions, which have attracted considerable attention, but still remain underinvestigated.

CHAPTER V

Experiment: Long-Plasma-Scale-Length Solid Target Interaction: Proton Acceleration

The recent observation of hot protons [10, 25, 36] from ultrahigh-intensity laser and thin film target interactions has generated great interest in applying these beams in a multitude of research areas, including dense-plasma diagnostics [37], radiography [12], radiation therapy [7], radioisotope production [39], table-top nuclear reactions [41], nuclear physics [9], compact neutron sources [44], light ion fast ignition fusion [8], and even space propulsion [28]. These applications require good control of the proton beam characteristics, which remains underinvestigated. This chapter focuses on the target material effects on proton acceleration in order to explore the traverse motion of electrons and protons inside the target plate.

5.1 Experimental Setup

This experiment uses a T^3 laser system in University of Michigan. The laser system and experimental setup are shown in Chapter III. At the diagnostic area, two detectors are installed, one is RCF; the other one is CR-39. CR-39 is a transparent plastic nuclear track detector that is sensitive to all the particles, such as protons, helium ions, and carbon ions. Charged particles, passing through the CR-39 sheets, can damage the polymeric bonds; it is possible to highlight this damage with an

appropriate chemical etching. After etching, the particle paths look like pits (or holes) because of the linear track loss of the particle energy. The CR-39 is capable of recording ions with energies of 100 keV/nucleon. The electric charges and the energy loss of the particles are determined from measurements of the pits' base area and depth of the pits.

There are two kinds of etching processes: slow and fast etching. Slow etching, which requires 160°F incubation for six hours, does not need as high a temperature as a 6.25N NaOH solution, but requires longer time. In general, these two etching processes provide similar charge resolution of the pits. Therefore, each charged particle leaves a track on CR-39 if the energy is above 100 keV; however, a saturation of the visibility of the tracks is reached beyond a certain point.

As seen from the experimental results, when the number tracks on the CR-39 exceeds 6×10^6 particles/mm^2, the tracks become too crowded to be distinguished. See Fig. 5.1. This is called CR-39 bleaching effect. To avoid this effect, decreasing the etching time by using a fast etching process or inserting filters to filter out some low energy particles can be used. To obtain the flux information, putting the CR-39 under a microscope and manually counting the number of tracks within one unit area is typically done.

In our lab, we replaced the lamp inside the normal flat back scanner with a laser light source. This replacement introduces coherence to the scanning procedure by allowing better reflection of the light, which is what the scanner detector detects. This method also provides a good measurement of the bleaching effect area, see Fig. 5.1.

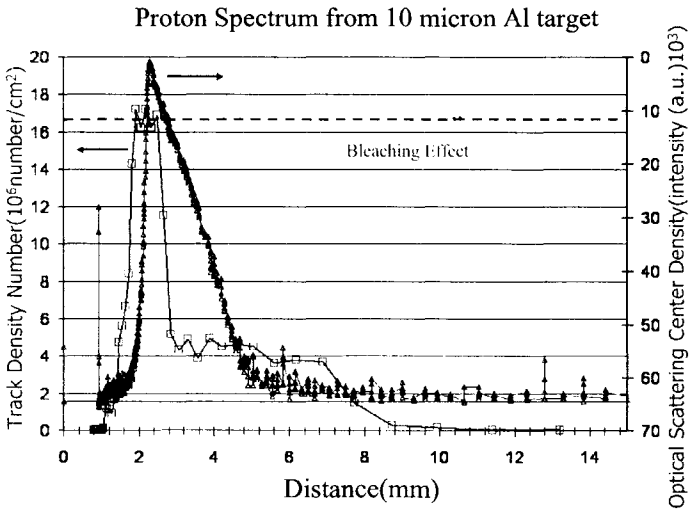

Figure 5.1: A comparison of a track counting method and the laser light source densitometer results.

5.2 Origin of Protons from the Ultrahigh-Intensity Laser and Solid Target Interaction

Previous experiments [39] using thin targets that are coated with deuteron-activated boron-11 have shown that the majority of high-energy ions originate from a front surface contamination layer. These front-side protons can be accelerated from two locations: (1) at the critical surface [24], due to charge separation by laser ponderomotive forces; and (2), from the interface of the front-side plasma and the solid dielectric bulk, due to stochastic heating of the electrons by a standing wave created by the incident laser pulses and reflected laser pulses in the underdense plasma plume [47]. The protons and other ions are accelerated to MeV energies through the target by the huge electrostatic fields. But the heavier ions can traverse only through the thinnest targets, due to their large energy losses.

Protons from the rear surface also have been reported [25], which are accelerated by the proposed target normal sheath acceleration (TNSA) mechanism. Achieving rear-side acceleration requires sufficient electron propagation through the target in

sufficient numbers to establish the field at the rear side. Combining these two mechanisms of proton acceleration, the "Modified TNSA mechanism"(see Chapter ??) is formed.

Different origins of protons also can be reflected into the proton beam. For example, a recent publication compared proton beams from metal and plastic targets [18, 45] and concluded that their differences could be attributed to the geometry of the targets and the intrinsic ability for electron transport. This chapter reports the experiment on the target material effects on proton beam profile quality; the target thickness also is a related key to influencing on the proton beam profile. A simulation result will be shown to provide a qualitative comparison of the proton beam structure to an electron beam simulation by Gremillet *et al.* [21].

An experiment to verify the origin of the proton acceleration is conducted by coating deuterons on the target surfaces. A Thompson Parabola (TP) is used to detect the ions coming out of the target. See Fig. 5.2. The TP can distinguish the ion species by adding both an electric field and a magnetic field to differentiate charge-to-mass ratio species.

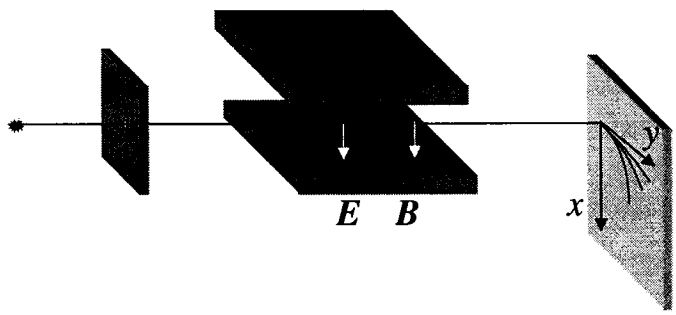

Figure 5.2: A schematic diagram of the Thompson Parabola.

Fig. 5.3 shows the CR-39 images that are installed at the back of the TP shown in

Fig. 5.2. These CR-39 slides show the relative contribution of the front-side proton acceleration to the ion distribution. There is a very strong deuteron component from the front-side, which is also higher in energy. These data show that the deuteron signal is strong from the rear in thicker targets, but the front also contributes to the proton acceleration, and a recent publication also agrees with this measurement [19].

For thinner targets, the rear sheath is disrupted by the prepulse preheating and burning-through the target. On the other hand, for 12.5 μm aluminum and 13 μm mylar targets, a more pronounced deuteron peak from the rear side coating is observed. This indicates at T^3 laser conditions, 6μm thick targets suffer the burn-through. The 13 μm thick targets may be the optimal thickness for rear-side proton acceleration, the higher proton energy source. In Fig. 5.3, the plume on the right shows multiple C^+ and O^+ species, from C^{+5} to O^{+5}. We never observed C^{+6} in any of our shots. Accordingly, this is good evidence of the "Modified TNSA mechanism" in our laser conditions. Note that the deuteron and C^{+6} have the same charge-to-mass ratio, but ionizing both the L-shell electrons requires greater energy. The deuteron parabola traces in Fig. 5.3 are very pronounced compared to other carbon species traces. Therefore, the traces in Fig. 5.3 are deuteron traces.

5.3 Electron and Proton Transport in Conductors and Insulators

Due to the electrostatic field, which is built up by the electron and ion separation, the movement of the electrons is considered the main factor affecting both the spatial profile and the energy spread of the accelerated proton beam. The behavior of the electrons is governed by Ohm's law, $j_r = \sigma E_b$, showing the relationships among between conductivity, the electric field, and free-space current in static state. Appreciable transport of such currents can occur only if the background target elec-

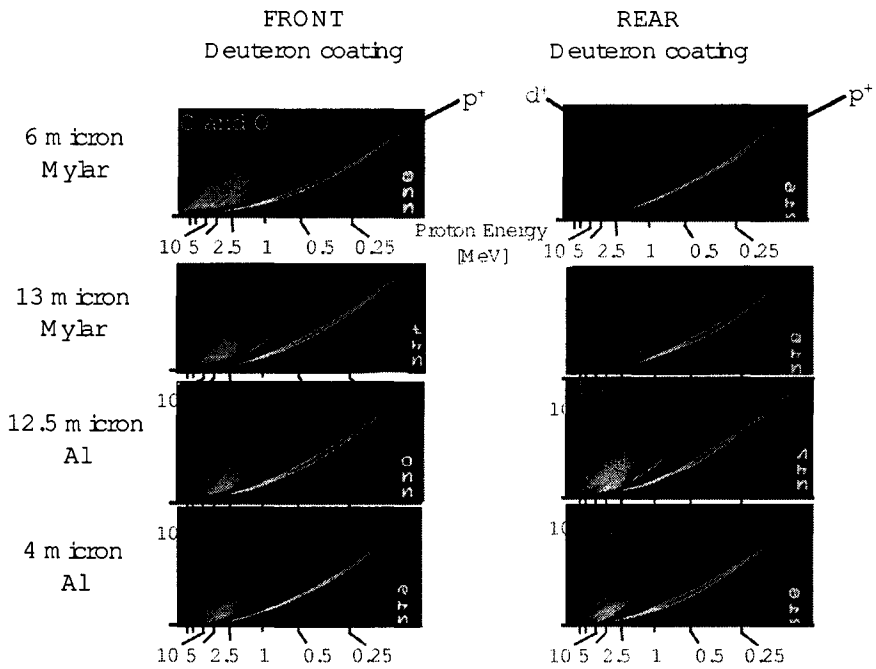

Figure 5.3: CR-39 scanned images showing the front side and rear side proton acceleration.

trons provide almost complete neutralization by return current in collisional plasma, which also obeys Ohm's law. However, when the return current is not equal to the forward electron transport current, conductivity σ changes value across the cold solid target and warm-dense plasma interface. Therefore, we can conclude that conductivity plays an important role in the electron transport process. Namely, when the conductivity is low, the return current suffers larger resistivity due to the lack of available free-charge carriers, and the propagating beam quickly loses energy from strong Ohmic dissipation. A schematic plot is shown in Fig. 5.4. As shown on the right hand side of the figure, without this charge neutralization, the electric field begins to ionize the bulk dielectric. This leads to beam instabilities, as seen in a recent simulation [21] that modeled electrons propagating through a silica target, under similar conditions to our experiment.

Why would the return current in conductors be able to provide support to forward

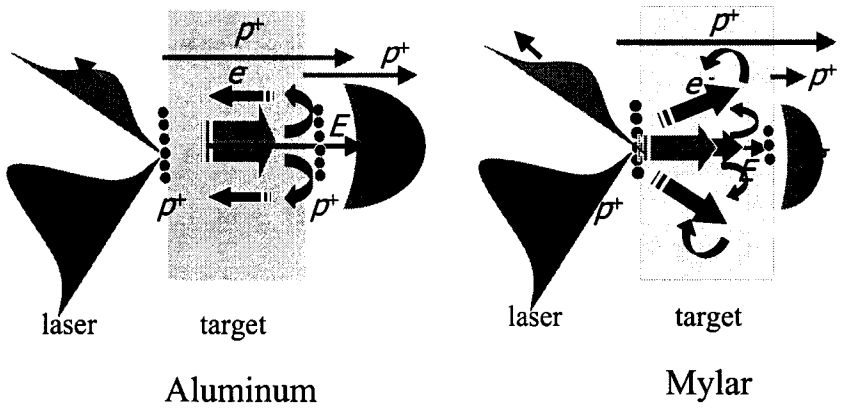

Figure 5.4: Conductor v.s. Insulator

electron transport? The key is the magnetic field. When the number of forward-propagated electrons penetrate through the solid target, a magnetic field is induced. However, this magnetic field potential is the force that prevents the electron forward transport inside the target. Inside the conductors, more free carriers can transport return current, and the magnetic field generated from return current has the opposite sign compared to the one forward-propagated current generated. These two magnetic fields cancel each other; as a result, in conductors, electrons are easier to propagate through the target because insulators have no return current to cancel out the self-induced magnetic field. As we can imagine, a lower number of electrons with lower energy are generated, so that fewer and lower energy of protons are accelerated from insulator targets.

In terms of spatial profiles, because the electron response from insulators is not linear, the accelerated proton beam's profile also reflects the nonlinear nature of the target. For conductors, the proton beam shows the homogeneous nature of the target. See Fig. 5.5.

Fig. 5.5 shows the different spatial profiles of proton beams. All pairs are from single shots, except (c)-(d), whose images consist of two separate shots. The RCF

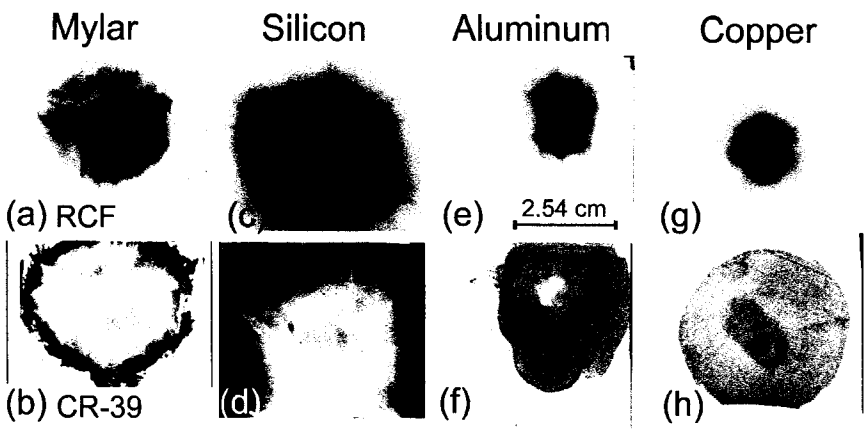

Figure 5.5: Spatial profiles of proton beams. The upper row is the RCF real image. The lower row is the scanned image of CR-39 detector stack. From left to right are shown materials of increasing electrical conductivity, from Mylar to silicon, aluminum, and copper. Vertical image pairs show the same laser shot data, although the RCF is put on top of the CR-39, which results in the different energy range of these two images. (a)-(b) shows 13-μm thick Mylar; (c)-(d) shows 12-μm silicon targets; (e)-(f) shows 12.5-μm aluminum targets, and (g)-(h) shows 12.5-μm copper targets [16].

images (a),(c),(e) and (g) show protons of $\sim$ 0.2 MeV to $\sim$ 1.4 MeV. The CR-39, images (b),(f) and (h) show protons of $\sim$ 2.5 MeV to $\sim$ 6 MeV, and (d) $\sim$1.2 MeV to $\sim$ 5 MeV. The darker oval central region in (h) is from protons with energies above $\sim$10 MeV exposing the rear of the slide. The whiter area in the center of the CR-39's image is from the bleaching effect of CR-39. At these regions, the track density is larger than 6×10^6 particles/mm^2; therefore, when the CR-39 piece is scanned by a normal flat back scanner, the tracks transmit or reflect more light. From this figure, we can see that when the conductivity is larger, there is a more smooth spatial profile of the proton beam.

In addition to the beam's smoothness, we also observe a proton beam ring structure from both conductors and insulators. The evidence of micro channeling can be seen in the data from the thinnest targets in Fig. 5.6, which display remarkable similarities to each other: mylar I (a), 6 μm; aluminum III (a), 4μm; and mylar III (c), 25 μm. The ring patterns on the RCF is an indication of beam hollowing from the

electrothermal instability that is predicted by Haines [22] and seen in the simulations by Gremillet *et al.* [21]. As the electron beam propagates through the solid, the conductivity becomes a factor with respect to the current. The on-axis part of the beam heats most significantly, reducing the resistivity, and allowing a return current to flow on-axis. This return current cancels out the forward propagated beam to form a hollow region, known as beam hollowing effect. Front-side protons effectively see no potential on-axis. The sheath for the TNSA mechanism tends to spread itself out on the rear surface, smoothing out the effect on any rear-side accelerated protons. Thus, we can say that these rings are due to protons coming from the front surface.

In conclusion, the target material conductivity can have influence on the output proton beam in three respects. (1) the proton beam's maximum energy is higher from conductors; (2) the spatial profile is less structured and more uniform in conductors; (3) the angle of divergence is greater at higher energy protons in insulators. However, the proton beam from conductors and insulators share the same feature of the hollowing effect.

5.4 Target Thickness Effects

From the electron transport point, above, we would think the distance the electrons need to travel through the inside of the target material might affect the characteristics of the output proton beam. Fig. 5.6 shows the spatial profiles of proton beams from Mylar and Aluminum targets in different target thicknesses.

In Fig. 5.6, images are formed on RCF from protons with energy between ~200 keV and ~1.2 MeV. CR-39 images are formed by protons greater than ~2.6 MeV to ~5 MeV. On both RCF and CR-39 images, the effect of target thickness is that the beam size becomes smaller as the target thickness increases. This effect is due

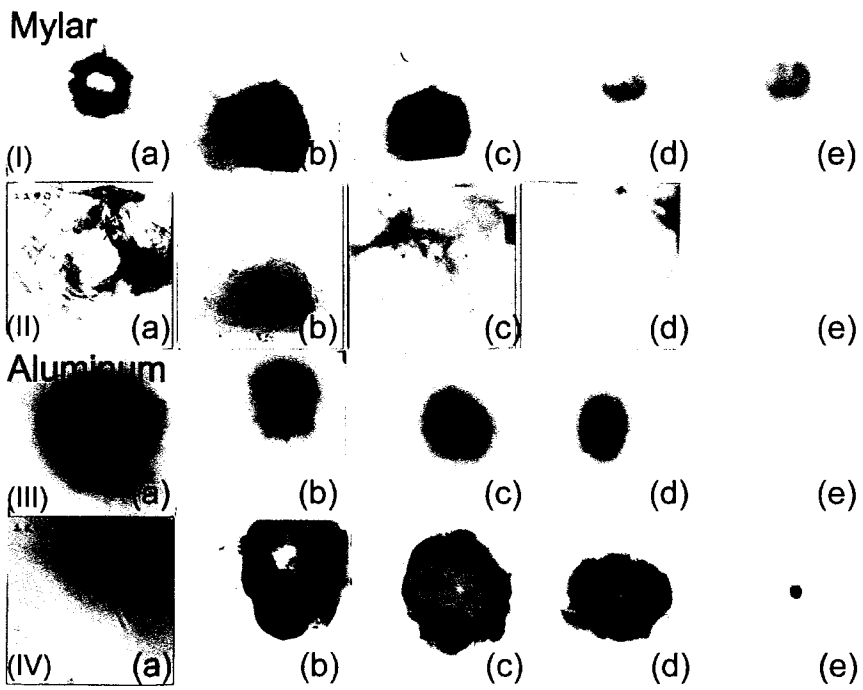

Figure 5.6: Proton beam on RCF and CR-39 images. Rows (I) and (III) are RCF real images. (II) and (IV) rows are CR-39 images, where (I) and (II) pairs show the data at the same shot from mylar targets with different thicknesses: (a) 6-μm, (b) 13 μm, (c) 25-μm, (d) 50-μm, (e) 100-μm; pairs (III) and (IV) show the data at the same shot from Aluminum targets with different thicknesses: (a) 4-μm, (b) 12.5-μm, (c) 25-μm, (d) 50-μm, (e) 75-μm [16].

to changes in electron transport. Because the laser on-axis direction has higher energy electrons in thicker targets, the outer ring of the electrons cannot propagate through the whole target thickness. This target thickness significantly reduces the forward-propagating electrons, which drives proton generation. Therefore, with thicker targets, smaller proton beams are accelerated. The proton beams from mylar targets also have the same features.

Section 2.3.3 showed the significance of the recirculation electrons. As we can see in this section, the thickness of the target can determine the recirculation of electrons as well [35]. Fig. 2.3 illustrates that the hot electron bunch length is approximately the same as the laser pulse length, L_p, because the velocity of these hot electrons

is approximately the velocity of light, c. The bunched electrons travel through the highly conductive target, like a metal or a plasma, without energy loss. They are then reflected at the target surface by a self-induced sheath field.

When the target thickness, L, is greater than half of the pulse length, $L_p/2$, as seen in Fig. 2.3, the electrons overlap only locally at the target edge and there is no significant increase of hot electron density. When $L < L_p/2$, the electron recirculation can provide an increase of electron density. Note that the electron recirculation can only increase electron yield but not increase the electrons' energy. The hot electrons do not lose energy inside the target; they circulate continuously until they transfer their energy to the protons.

For the T^3 400 fs laser pulse duration case, the L_p=60μm. Therefore, if the target is thinner than 60μm, the electrons can circulate more times and transfer more energy to the protons. The circulation electrons' effect can be observed in the proton energy versus target thickness plot in Fig. 5.7.

Fig. 5.7 is a very important experimental plot in proton acceleration research, especially as evidence of the "Modified TNSA Mechanism." From this plot, three kinds of data trends are observed: (1)when the target thickness is thinner than 13μm, the maximum proton energy dropped significantly with thinner target thickness; (2)when the target thickness is thicker than 13μm but thinner than the LET loss effective thickness, the maximum proton energy starts to drop when the target is thicker; (3)when the target thickness is thicker than the LET loss effective thickness, the corrected maximum proton energy stays the same when the target is thicker.

At region I in Fig. 5.7, the target is so thin that the laser-plasma interaction suffers target "burn-through." The target cannot withstand the huge field force from the incident laser pulse; the ion-wave induced shock wave destroys the thin solid

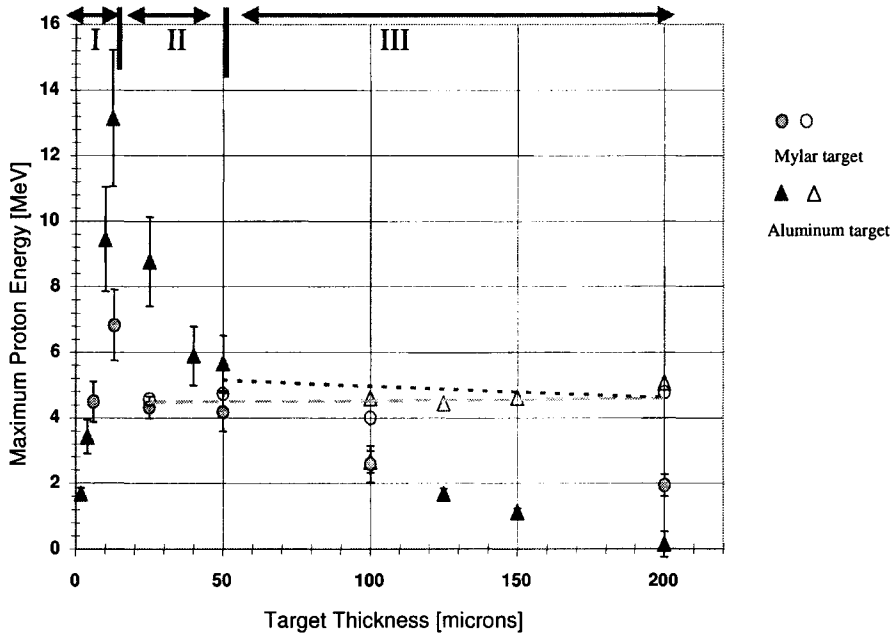

Figure 5.7: The relationship between maximum proton energy and target thickness. Blue triangles are aluminum target data; orange dots are mylar target data. Solid points are the experimental data; the open points are corrected for the particle Linear Energy Transfer (LET) inside the material at the same target thickness. The dashed line shows the corrected data trend beyond the point at which LET starts to affect the total energy output of proton beam [16].

target surface before the main pulse arrives. This process can result from a prepulse of the incident laser, which is produced by the incomplete compression stage. This effect significantly decreases the efficiency of proton acceleration, and the influence is more pronounced on thinner targets. The results show the thinner the target, the smaller the maximum proton energy.

Region II in Fig. 5.7 illustrates the "Modified TNSA Mechanism." When $L < L_p/2$, the electrons have more chances to recirculate with thinner targets so that more energy transfer from electrons to protons is completed and also more rear-side proton acceleration is achieved. As a result, maximum proton energy increases as target thickness decreases. For 13μm aluminum, a 13 MeV maximum energy of proton beam is generated, while for mylar targets, the maximum proton beam energy

is about 7 MeV.

At region III in Fig. 5.7, $L > L_p/2$, the electrons do not have enough strength to reach the rear side of the target and be reflected, so no recirculation currents are present beyond the $L = L_p/2$ point. Based on the TNSA, there should be a constant output proton beam in terms of maximum proton energy. However, for thicker targets, the charged particles will suffer the LET loss inside the material.

After the LET correcting of the proton energy, the constant maximum proton energy, as we expected, is observed at 5 MeV (shown as a dash line in Fig. 5.7). This implies an important result of metal targets: the target front side acceleration provides maximum energy of 5 MeV protons, which is without electron recirculation. On the other hand, the rear-side acceleration, for electrons having the greatest circulation without burn-through effects, the maximum proton energy is 13 MeV.

This trend is predicted by the simulation results as well [48], see Fig. 2.4. The mylar target shares the same features as the aluminum target, but, due to the lack of movable carriers to carry the electrons, the maximum energy is much lower than with the aluminum targets. Inside the mylar target, the LET loss is greater than inside the aluminum target so the maximum proton energy drops more significantly for mylar than for aluminum.

In conclusion, for targets thicker than $L_p/2$, thinner targets increase peak proton energy. For targets thinner than $L_p/2$, the thinner the target is, the lower the maximum proton energy is.

5.5 Particle Beam Filamentation

The RCF image in Fig. 5.6 I (b) displays a remarkable star-like symmetric structure similar to that in Fig. 5.5 (a) and (b). Due to the stochastic nature of the

two-stream and Weibel instabilities in the electron beam, we can observe some evidence of these instabilities in the RCF images of these structures in the proton beam. Fig. 5.6 (I) shows the evolution of the proton beam from a ring to a star, back towards a ring, and then a lobed structure. 3-D simulation results are shown in [21], demonstrating a ring pattern at thicknesses less than 20 microns in 3-D isosurface plots of the current (figure 5 (a) in [21]), as well as the magnetic field slices (figure 6 in [21]).

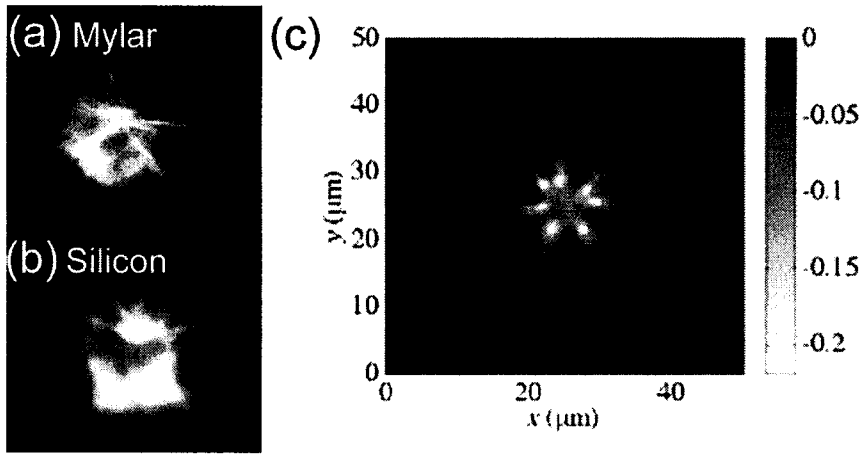

Figure 5.8: A comparison of simulation results (c) and our experimental data (a) and (b). This plot is adapted from [21] by permission.

The simulation results are of the electron beam transverse profile. Assuming electrons are driving the proton acceleration, the electron and proton beam profiles should share some similarities. With this in mind, Fig. 5.8 illustrates the similarities of the experimentally observed proton beams from (a) mylar and (b) silicon targets and the simulated electron profile (c) from [21] propagating through a silica target. The simulated electron beam had a 10μm FWHM Gaussian profile, a 405-fs rectangular pulse duration, an energy level of 500 keV, and a density of 10^{20} cm^{-3}. Inside the target plate, there is always resistive force that drags the propagating currents to lower velocity. The increased Ohmic dissipation results in increased magnetic field

generation by the earliest electrons entering the target, but creates some free electrons that can act as a cold background return current for the trailing beam electrons that are pulsed into the target.

The induced magnetic field grows larger after the electrons enter the target material; the magnetic field is then large enough to affect the trajectory of electrons. The electrons start to be bent by the field, but due to the velocity distribution of the electron beam, the electron beam starts to form a filament structure. In [21], a star-like structure of the electron beam is observed between 7 and 20 microns inside the target, as seen from the transverse direction, shown in Fig. 5.8 (c).

In addition to the star-like structure, some instability effects also are observed in our experimental results.

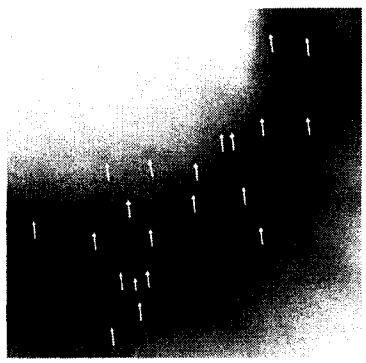

Figure 5.9: An enlargement of Fig. 5.6 I (a). The white arrows show the beamlets' structure.

The small dots on the RCF are filaments due to the two-stream or Weibel instabilities in the electron and proton beams. Fig. 5.9 shows an enlarged image of Fig. 5.6 I (a). The white arrows mark the presence of multiple beamlets inside the ring structure. The density of beamlets noticeably decreases toward the center of the ring with no beamlets present directly at the center of the ring, and none outside the ring.

5.6 Summary

From proton acceleration in the long-plasma-scale-length solid target interaction experiment, the origin of the proton source was explored, the mechanism of proton acceleration, the spatial profile of proton beams, and the conductor and insulator targets' effects on the proton beam. The conclusions about the proton acceleration are: (1) the higher energy protons are accelerated from the rear side of the solid target, while the lower energy portions are from front side; (2) the return current plays a critical part in the solid target experiment; (3) the target thickness plays an essential role in the proton acceleration: targets thinner than half of the pulse duration provide more chances for return currents to circulate to give higher proton energy output; (4) conductive targets can support smoother proton beam output than insulating targets; (5) instability-induced filamentation structure is observed.

This chapter included a thorough investigation of proton acceleration and presented good evidence to support the theory researchers have predicted, helping me to have better control of the laser-driven proton beam.

CHAPTER VI

Experiment: Short-Plasma-Scale-Length Solid Target Interaction: Prepulse Effects on Proton Acceleration

The relativistic intensity regime is rich in physical effects, including acceleration of electrons and ions to multi-MeV energies, vacuum heating at surfaces, relativistic harmonic generation from free electrons, and relativistic self-focusing of the laser light. When the laser intensity is high enough, not only do electrons become relativistic, but so do ions.

The acceleration of protons and other ions from plasmas produced by ultrahigh-intensity lasers is a rapidly growing research field at the present time. Due to the various applications, such as proton accelerators [10, 25, 36], proton radiography [4, 12], material science research, and possible radioactive sources for medical purposes [7], researchers are interested in optimizing the parameters of ion generation from the ultrahigh-intensity-laser overdense-plasma interaction.

Previous publications [11, 45] showed the influences of laser intensity and target materials on proton acceleration. M. Kaluza's report in Physics Review Letters, 2004 [27] suggested that the preplasma created by the laser prepulse is the key to affecting the efficiency of proton acceleration. The free electrons inside the preplasma is the main driving force for the proton acceleration; therefore, we need the preplasma. On the other hand, if the prepulse is higher than the ionization threshold of the solid

target material, a direct burn-through of the target will decrease the efficiency of proton acceleration.

In earlier experiments, an optimum magnitude of prepulse for proton acceleration was found; however, until now, a clear correspondence of preplasma expansion scale and proton acceleration efficiency has not been established. To optimize the parameters to provide greater efficiency of proton acceleration, a study of how protons accelerate from the prepulse and the solid target is necessary. As a result, a more efficient and smaller-sized proton accelerator can be developed.

This chapter presents the optimization and control of proton acceleration by exploring the effect that the preplasma creates.

6.1 Experimental Setup

To obtain quantified information regarding the influence from the known prepulse magnitude, an intensity-maintained and timing-controllable laser prepulse is needed. Unfortunately, there is already a prepulse of unknown intensity in front of the main pulse due to the incomplete compression process; to eliminate or diminish this unknown prepulse and introduce a controllable prepulse will be a priority.

In Chapter II, it has been shown that the ASE is the main source of the preplasma, and to eliminate this nanosecond-scaled ASE is very difficult for us. However, by utilizing nonlinear optics, reduction of the prepulse intensity to one over the square of the original magnitude is possible by doubling the frequency of the laser light. When this high-intensity laser pulse hits the nonlinear crystal, the frequency of the original laser is doubled.

Due to the fact that the laser pulses meet the Type 1 phase matching condition (two of the same polarized incident beams give out light beam with polarization that

is perpendicular to the incident beams), the nonlinear crystal generates the second harmonic, which has a doubled frequency. In T^3's case, the fundamental beam is at 1.053 μm; the second harmonic is at 527 nm. Although the second harmonic output still keeps some of the characteristics of the original pulse, the relative contrast is doubled. A similar experiment has been performed and published in [36], in which a contrast-improved doubling light was also used.

The relative contrast is important. Originally, the contrast of the T^3 laser was five orders of magnitude (Fig. 2.2). After doubling, the contrast ratio is ten orders of magnitude. If the intensity of the main pulse is 10^{19} W/cm^2, the pedestal intensity of the second harmonic beam is only 10^9 W/cm^2. This does not affect the solid targets, which have an ionization threshold of about 10^{13} W/cm^2. As a result, a "clean" pulse with 10^{19} W/cm^2 intensity is obtained. The experimental setup is shown in Fig. 6.1.

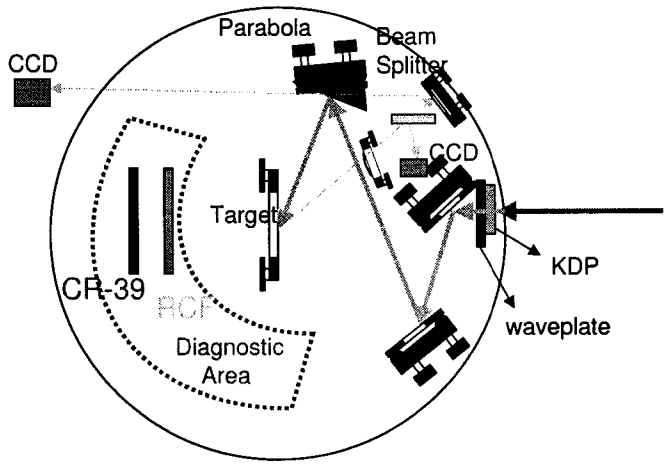

Figure 6.1: The laser prepulse experimental setup. The 2-inch fundamental laser beam goes through a 1/2 waveplate to rotate the polarization of the laser pulse to s-polarization and then passes through a 4mm KDP to double the frequency, producing p-polarization incident on the target plate. The frequency doubled light is focused by an f/2 dielectric parabolic mirror which is coated for 527 nm and 1.053 μm. A spotsize of about FWHM=3 μm is obtained on the target plate at the focal point.

The proton beam energy spectrum always has a clear cutoff at the high energy tail, which is expected by the acceleration mechanism as a result of an electrostatic field. In the diagnostic area, a CR-39 mounting wheel is installed with eight pieces of CR-39 per experimental run. The energy limiting filters are inserted in front of the CR-39 to filter out different energy particles before forming a track on the detectors.

6.1.1 Michelson Interferometer

After a frequency-doubled "clean" pulse is obtained, introducing the prepulse by inserting a Michelson interferometer is easy. A Michelson interferometer, which has two identical pulsed outputs (see the Fig. 7.1), is installed inside the laser chain to maintain the same amplification and compression for the prepulse and the main pulse.

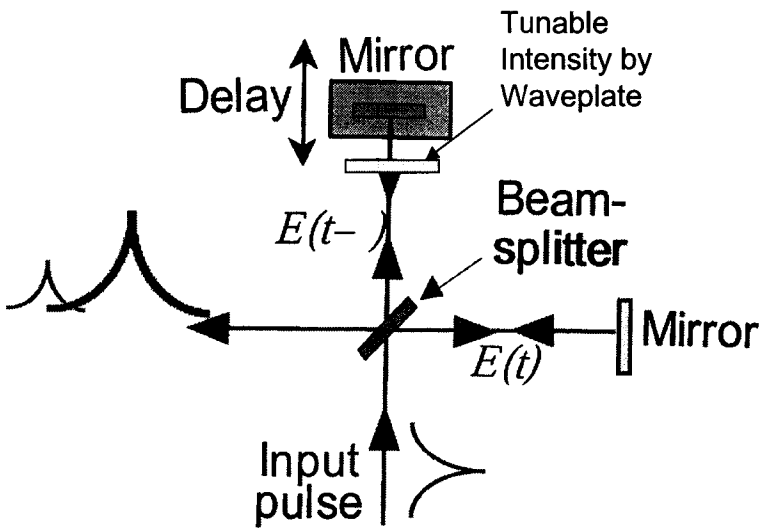

Figure 6.2: A Michelson interferometer is shown. The output beam will combine the pulses from the two perpendicular arms with a time delay which results from a distance difference between those two arms.

A waveplate and a polarizer are inserted into the adjustable arm that sets the intensity of the pulse. The timing of the arm is set by the translational position of the micrometer. At the other arm, a movable mirror is installed for alignment

purposes. CR-39 is used to record the energy of the protons that flow along the perpendicular direction of the target plate.

Note that the intensity of the pulses of each arm decrease to a quarter of the original pulse without a Michelson interferometer, due to the 50:50 splitting ratio of the beam splitter. This may cause the intensity to be too low. In the T^3 case, with full injection energy, a total of 4 J energy can be achieved before the compressor; after the compressor, a 50% efficiency compressor results in 2 J being thrown away; after the doubling crystal, another 50% of the energy is thrown away. As a result, only 1 J of energy can be focused at the target plate. After inserting the Michelson interferometer, only 250 mJ can be focused at the target plate. With a f/2 parabola, the peak intensity at the focal spot is only on the order of 10^{18} W/cm^2. This may not be allow enough dynamic range for the prepulse to be adjustable. Due to the fact that the losses in the compressor and losses from the doubling crystal are unavoidable, a harder amplification for the seeded pulse is needed.

The single-pass amplifier glass rod used in T^3 is Nd:Glass. Three amplifier heads are used in T^3 with aperture diameters of 16mm, 16mm, and 45mm. The heads are held at a high voltage to increase the energy transfer to the pulse when the rod discharges. Therefore, higher amplification can be achieved by increasing the rod voltage up to the medium's damage threshold. From the calibration experiments, a 500 volt difference on each head can result in 50% output energy difference at 2 J, indicating that even after the Michelson interferometer is inserted, if a 500 volts are increased at each head, a 4 J output energy level per pulse can be obtained. This voltage increase provides enough dynamic range to observe the proton energy changes at different peak intensities.

6.2 Measurements of KDP's Conversion Efficiency

To obtain a good estimate of the spot intensity on the targets, a conversion efficiency measurement is required. Note that this doubling conversion process cannot be 100% efficient, and there is a saturation point associated with a high incident beam intensity. The relationship between the second harmonic pulse energy passing through the KDP crystal and the energy of the laser pulse can be obtained, and a saturation plateau is observed. Nonetheless, if the incident beam energy exceeds 1 J on the KDP crystal, the high-intensity pulse will initiate a filamentation effect on the output beam, thus, affecting the ability to achieve tight-focusing. The focal spot, as a result, is distorted and can introduce unknown factors into the experiment. Therefore, to avoid a wavefront-distorted focal point and the energy level drop after the nonlinear crystal, pre-calibrating the laser output energy is necessary to avoid reaching the saturation point.

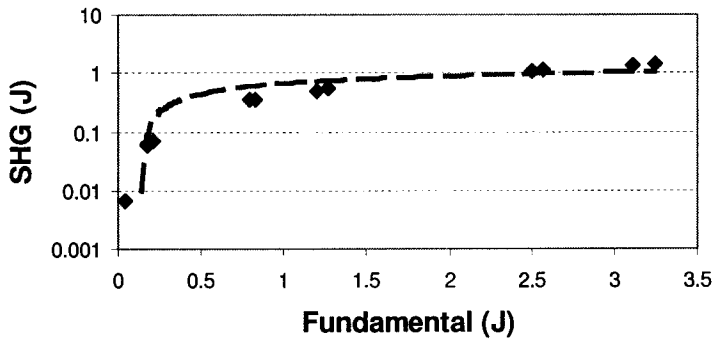

Figure 6.3: SHG output vs. fundamental input. This plot shows that the SHG has a saturation value when the fundamental input reaches a threshold.

In Fig. 6.3, saturation is observed after the input fundamental pulse power reaches 1.5 J. In Fig. 6.4, the best Second Harmonic Generation (SHG) conversion efficiency is reached after the input is above 0.75 J. This trend indicates that if the incident pulse is above 0.75 J, the conversion efficiency is always 45%; however, when the

input pulse energy is above 1.5 J, the output energy will not keep increasing, but saturates at around 1.1 J. Although this saturation sets an upper limit of the focal spot intensity, it helps to prevent exceeding the filamentation threshold of the nonlinear crystal. When the incident field of the nonlinear crystal is too large, the higher order nonlinear coefficients need to be taken into account. Accordingly, small scale self-focusing occurs. The output SHG wavefront is not uniformly flat; instead, it shows filamentation.

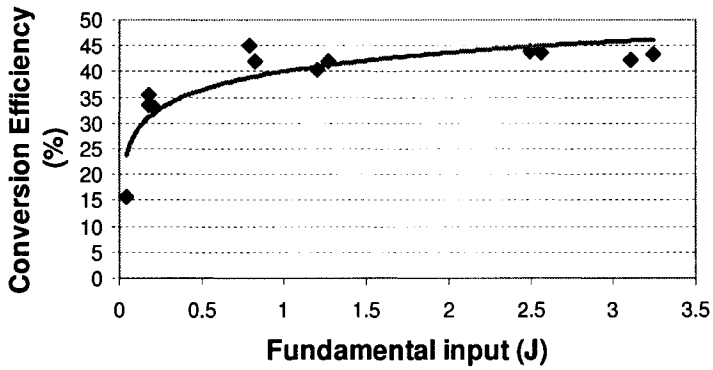

Figure 6.4: Conversion efficiency vs. fundamental input. A 45% conversion efficiency is observed after the saturation.

The SHG energy conversion efficiency also is studied as a function of the crystal angular mismatch. The tilt sensitivity of the Type I nonlinear crystal is shown

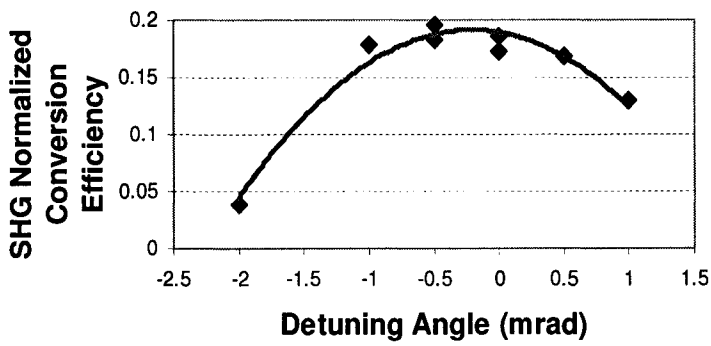

Figure 6.5: SHG output vs. mismatch angle. Normalized conversion efficiency of 4 mm KDP Type I crystal as a function of angle detuning plot.

in Fig. 6.5. It is measured by rotating the crystal horizontally along the incident

plane, which means the laser incident direction is normal to the incident plane. Theoretically, the detuning curve relative to the output energy is $\sin^2(\frac{x}{x^2})$ if the detuning angle is small enough to use small angle approximation, where x is the arc length of the detuning sector. Note that the crystal is expected to be more sensitive to the phase-matching angle for higher-intensity interactions due to higher order nonlinear coefficient effects.

As a result, a 45% conversion efficiency is the optimum second harmonic signal. The laser pulse energy is 3.5 J before the compressor, 1.75 J after the compressor, and 0.85 J after the doubling crystal. With a focal spot diameter of 3 μm, the peak intensity at the focal spot is 2×10^{19} W/cm^2. This intensity is enough to accelerate particles and observe a large dynamic range of the proton maximum energy.

6.3 Maximum Proton Energy Dependence on Target Thickness

To verify the contrast of the incident laser, aluminum samples of thicknesses from 0.8 μm to 200 μm were used as targets to find the relationship to maximum proton energy. Being able to accelerate protons to higher energy levels against thinner targets is strong evidence that the laser pulse is "clean" for proton acceleration.

If the foil is burned through by the laser prepulse, the acceleration field at the back side of the foil must vanish. As a consequence of the vanishing of the field, the proton energy must drop with decreasing foil thicknesses [63]. Accordingly, the smaller prepulse can make thinner targets bearable to the pulse pressure coming from the incident pulses. This indicates that the highest proton energy peak falls at thinner thickness, while the incident pulse has a better intensity contrast.

Note that from previous results [33], metallic targets can provide higher energy and smoother proton sources from the laser-matter interactions. Aluminum is rea-

sonably priced and is a good target material in terms of target flatness,thickness, and purity. Therefore, aluminum is chosen as the target material in order to have a larger range in which to see the energy changes of protons.

Fig. 6.6 shows the experimental data of the proton energy dependence on target thickness.According to the data, thinner aluminum targets give higher proton energy.

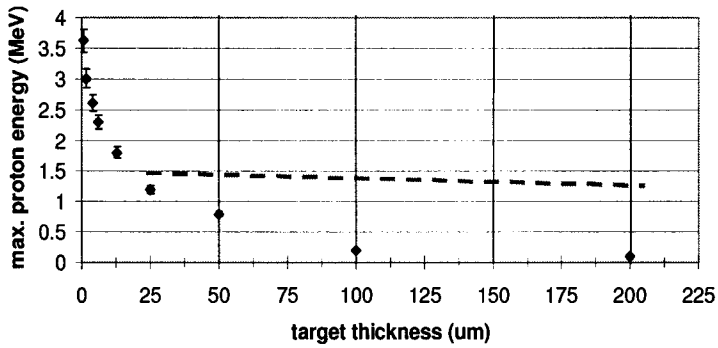

Figure 6.6: Maximum proton energy vs. aluminum target thickness. This plot shows that the proton energy is greater with thinner targets.

In Fig. 6.6, the blue dashed line is the corrected data from LET loss (see section 5.4) inside the target material, which shows the same behavior as in Fig. 5.7 except there is no region I (there is an energy drop when the target is thinner than 6 μm, as shown in Fig. 5.7). Region I exhibits the burn-through effect. Therefore, the lack of region I is good evidence that the laser pulse has a high contrast ratio. In other words, for a fixed prepulse duration, the highest proton energies are obtained at an optimal target thickness, which, in turn, is determined by the prepulse duration and intensity. This is known as laser contrast. The results can be consistently interpreted if one assumes that above the optimal thickness the fastest protons are accelerated at the target rear side, while for thinner targets only the front side acceleration is active, resulting in lower proton cutoff energies.

6.4 Laser Prepulse Effects

Unlike the low contrast case [33], in the high contrast cases, also the short plasma scale length cases, the optimum target thickness is thicker. This attracted the attention to explore how the prepulse affects the proton energy and optimum thickness of target plates. Thus, a prepulse was introduced into the original pulse study the effect. Besides changing the delay timing and the intensity of the prepulse, different target thickness effects also have been explored.

Two plots are shown in Fig. 6.7, and Fig. 6.8with two different target thicknesses (0.8 μm and 4 μm) and different prepulse delay times.

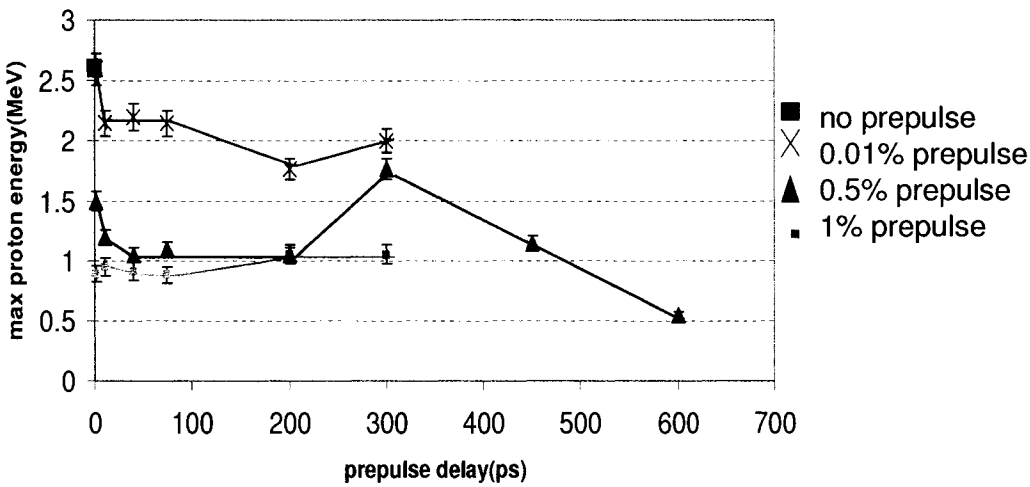

Figure 6.7: 0.8 μm prepulse delay scan. This plot shows the relationship between proton energy and prepulse delay and intensity with the 0.8 μm aluminum target. The green dot shows the proton energy without prepulse and the same intensity main pulse; the blue diamond shows a prepulse intensity of 10% relative to the main pulse; the yellow triangle is with 0.5% prepulse; the red cross is with 0.01%; the pink square is with 1% prepulse intensity. The corresponding colored line is the proton energy trend line to help observe the prepulse intensity effects on the maximum proton energy.

The significant changes in proton spectra and beam profiles described above can be interpreted as a transition between two regimes delimited by the optimal thickness: (1) Only the front side acceleration is active for targets thinner than the optimal

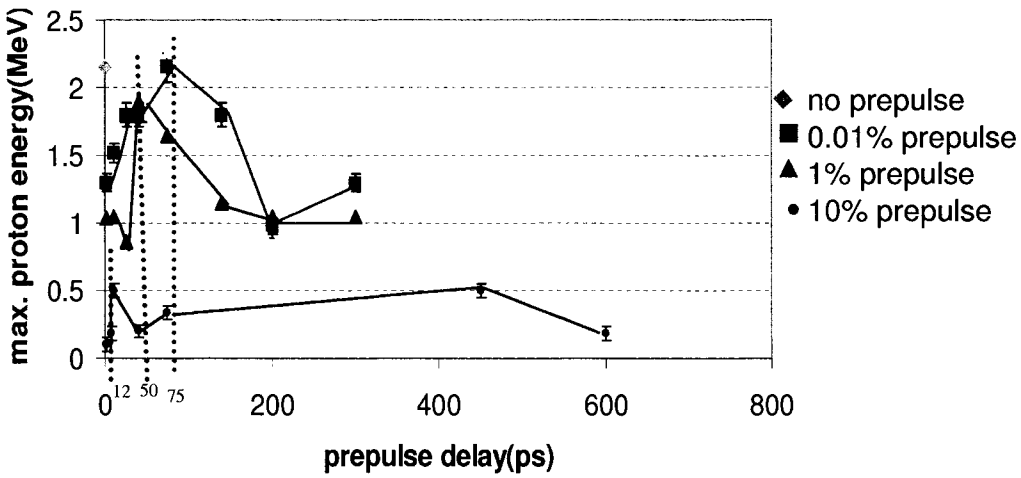

Figure 6.8: 4 μm prepulse delay scan. This plot shows the relationship between proton energy and prepulse delay and intensity with the 4 μm aluminum target. The pink diamond shows the proton energy without prepulse and the same intensity main pulse; the purple circle shows a prepulse intensity of 10% relative to the main pulse; the blue triangle is with 1% prepulse; the red square is with 0.01% prepulse intensity.

thickness and (2) protons are accelerated from both target surfaces for target thicknesses above the optimal value. In the second regime, the rear side acceleration leads to higher cutoff energies.

Typically, the electron cloud occupies a half cycle of the laser wavelength, whereas the penetration (effective skin depth) of the laser into the target is only a small percentage of the wavelength. From the plot in Fig. 6.7, a trend of lower and lower maximum proton energy is observed from the least prepulse intensity, 0.01% of the main pulse, to the largest prepulse intensity, 10% of the main pulse. It shows clearly that the preplasma is bad for proton acceleration even farther than the plasma scale length, which indicates the target plate is too thin to endure the prepulse's photon pressure and is burned through by the prepulse. As a result, when the main pulse arrives, the target is no longer flat and uniform. Electrons cannot accumulate in the rear surface of the target to form an electrostatic field; consequently, not as much proton acceleration can be accomplished. Hence, the 0.8 μm target is too thin for

the prepulse study.

From the 4 μm target data, more interesting results can be observed: the optimal value of the maximum proton energy is a function of the prepulse delay timing. In Fig. 6.8, four different prepulse intensities were tested, where pink diamond is with no prepulse; the purple circle shows a prepulse intensity of 10% relative to the main pulse; the blue triangle is with 1% prepulse; the red square is with 0.01% prepulse intensity.

These data show the trend that at thicker than 200 μm target thicknesses follow, the smaller the prepulse is, the higher the maximum proton energy is. However, the blue triangle and the red square series have a pronounced peak at thinner target thicknesses, especially for the blue triangle series. The prepulse intensity of the blue triangle is 1%. This is a hint that the plasma expansion condition at 1% prepulse intensity with short prepulse delay, 75ps, may be good for proton acceleration. On the other hand, these three different prepulse intensity series share one feature: a peak close to the zero prepulse delay; however, the peak position and the peak width are different. See Table 6.1.

$I_{prepulse}$ W/cm^2	Proton Energy Peak	Peak Width	Max. Proton Energy	C_s(μm/ps)	Preplasma Scale Length
10^{14}	75ps	160ps	2.2MeV	0.16640	~7 μm
10^{16}	50ps	75ps	1.8MeV	0.26310	~10μm
10^{17}	12ps	18ps	0.5MeV	0.37208	~15 μm

Table 6.1: Table shows three different prepulse intensity observations and their corresponding characteristics. The first red row summarizes the 0.01% prepulse intensity series; the second blue row summarizes the 1% prepulse intensity series; the third purple row summarizes the 10% prepulse intensity series.

When the prepulse intensity is larger, the proton energy peak happens when the prepulse and the main pulse are closer to each other; the peak width is smaller in larger prepulse than smaller prepulse cases. This is a good indication of the movement of preplasma. Besides, this result provides supports to the optimal condition of proton acceleration: (1) rear-side density profile is important for proton acceleration; (2) the coupling efficiency between laser pulse and electrons in the plasma depends on the gradient of the electron density profile; (3) the balanced point between rear-side disturbance and energy conversion efficiency is the maximum proton energy peak's location.

When the prepulse hits the target surface, the rear surface profile is disturbed. Therefore, when the main pulse arrives, the proton acceleration efficiency is decreased. However, after a longer delay between the prepulse and the main pulse, the front side preplasma has some time to expand. The slope of electron density at the front end becomes smaller, and this smaller slope of the plasma can couple more energy from the laser pulse into the plasma. As a result, in Fig. 6.8, proton energy becomes higher for all of these data series with longer time delay. But unfortunately, with 4 μm thickness aluminum, the energy conversion efficiency still cannot compensate the rear-side density profile disturbance; therefore, the peak of maximum proton energy is only equal to the no-prepulse case. It is expected that with thicker targets, a higher proton energy can be obtained with the same laser conditions.

In addition, because the smaller prepulse induced preplasma has smaller expansion speed (see Table 6.1), the optimal delay between prepulse and main pulse should be longer, and it is also observed in Fig. 6.8. Consequently, the proton energy peak is wider than the larger prepulse cases. Namely, the preplasma scale lengths are investigated in Adumi *et al.*[1], and the observations in [1] agree with our measurements

as well. Both of the results show that the process of resonance absorption is not very efficient for very short, clean (prepulse free) laser pulses, as it needs an optimum plasma scale length.

The prepulse-induced electrons first are driven by the ponderomotive potential $\psi_p = m_e c^2(\gamma_{os} - 1)$, where $\gamma_{os} = \sqrt{1 + I_L \lambda_L^2 / 1.37 \times 10^{18} (W cm^{-2} \mu m^2)}$ until the electrons' kinetic energy stand balanced by the electrostatic field by charge separation. m_e is the electron mass; I_L is the laser intensity; λ_L is the laser wavelength.

Furthermore, the proton acceleration time can be calculated as $\tau_a = \frac{\lambda_L}{c}\sqrt{\frac{m_p}{m_e \gamma_{os}}}$. With T^3 laser system, the acceleration time is 46 fs, which is much shorter than the laser pulse; therefore, protons have enough time and can initially gain kinetic energies approaching this potential [48]. Within the first 46 fs, the protons are accelerated to form a sharp wave front, but afterwards the repulsion force inside the wave expands the ion wave front. This process also can result in an increased maximum proton energy of about 50% [48]. Nonetheless, the pre-ionized electrons density profile, which the prepulse introduced, is the main parameter to determine the electrostatic field strength. It is the key factor in affecting the movement of the proton harp wave front. Thus, at our laser condition, 75ps prepulse delay and 1% prepulse intensity is the optimum for proton acceleration.

6.5 Summary and Future Work

This chapter illustrates the prepulse effects on the maximum proton energy: a prepulse with about 1% of main pulse intensity at 75 ps before the main pulse may be the optimal condition for the proton acceleration. The result is within my expectation due to the fact that the proton acceleration needs a certain amount of electrons from the plasma to be separated from the ions to establish the electrostatic

field inside the target plate that drive the protons out of the target. However, this amount cannot be too large or it destroys the structure of the target surface.

On the other hand, different prepulse intensities reflect different optimal prepulse delay timings, which shows that smaller prepulse intensity has shorter optimal prepulse delay time. This new result relates to the changes of the scale length with different plasma temperatures. Unfortunately, as you can see, still more investigation at shorter prepulse time delays need to be measured. Moreover, the preplasma expansion behaviors are always the issue for experimentalists to examine. No matter what the x-ray intensity, it provides an indirect measure of the plasma expansion behavior. The 2D hydrodynamic simulation can be used to verify the assumptions of this experiment.

CHAPTER VII

Experiment: Proton Beam Applications

Due to their particular properties, the beams of the quasilaminar, multi-MeV protons generated during the interaction of ultraintense ($I=10^{19}$ W/cm^2) short pulses with thin solid targets are best suited for use as a particle probe in laser-plasma experiments. This chapter presents two proton beam applications that take advantage of either the small-source or compact characteristics of the proton beam.

First is proton radiography. The recently developed proton imaging technique uses the beams for point-projection imaging as a diagnostic tool for detecting electric fields in laser-plasma interaction experiments.

Second is medical proton radiotherapy. In radiation therapy for cancer, using proton beams provide the possibility of better dose conformity on the treatment target compared to commonly used photon and electron beams because of the small emittance of the beam and the Bragg Peak effect. The compactness of the laser-driven proton beam can provide better clinical usages. From the preliminary results shown in this chapter, these two applications' although under investigation, have very promising possibilities for development and improvement in the future.

7.1 Proton Radiography

Previous chapters illustrated the mechanisms, characteristics, and controls of the proton beam accelerated by ultrahigh-intense laser and solid targets. The properties of the proton beam are of interest for a number of important applications, which include the ignition of compressed fusion capsules [46] and probing of laser-plasma experiments [4]. Namely, the point-projection imaging scheme as a diagnostic tool is an advantage, and high spatial resolution is achievable [5] by back-illuminating an object with the proton beam. In a point-projection imaging scheme, this emits the beam from a source with a radius of a few microns. This section presents a preliminary result for proton radiography uses.

7.1.1 Experimental Setup

Using the five-order-contrast laser, the proton beam images are scanned onto RCF and CR-39 film. The laser condition is shown in Chapter III. A schematic od the setup after the solid target is shown in Fig. 7.1.

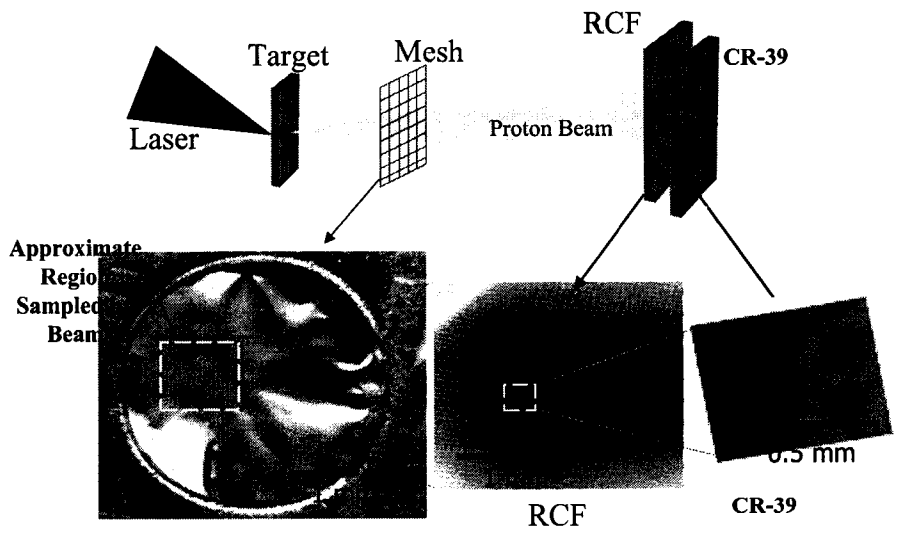

Figure 7.1: A schematic figure of the proton radiography experimental setup and RCF and CR-39 scanned images [16].

The proton beam is detected by RCF and CR-39 pairs. The RCF is put on top of the CR-39 detectors. In the experiment, the proton source (from a 13 μm aluminum target) probes objects. The objects can be called "masks." The mask in this experiment is a copper mesh, 10 μm thick wire with 30 μm spacing. Even with thin masks, strong modulations of the masks can be imprinted in the proton beam where the collisional stopping of protons is negligible.

The modulations arise from multiple, small-angle scattering in the mask, which increases the local divergence of the beam. Therefore, the dark and bright proton beam shadows can be observed after the mask. In cases without collisional stopping, this effect can produce a high-contrast, magnified shadow on the mask. See Fig. 7.2.

7.1.2 Proton Source Measurement

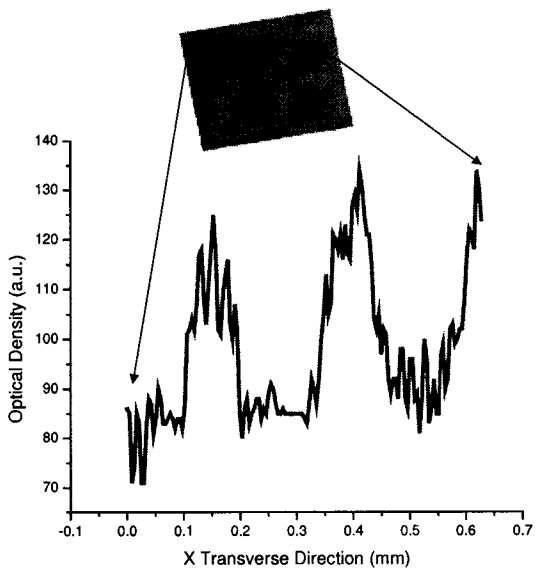

Figure 7.2: The lineout in optical density of the CR-39 images of the magnified mask images.

As shown in Fig. 7.2, the modulations in each grid structure is due to the light transmittance of a single proton particle track on the CR-39. Each track on the CR-39 can transmit light, but the wall of each track may block some light transmission.

Regardless, a clear mesh shadow still can be easily observed.

The geometric magnification should be seven times, which is M_G=L/d, where L is the distance between the target plate and the detectors, and d is the distance between the target plate and the mask. However, from the images of CR-39 in the experiment, the magnification is M_{exp}=3.3, which is smaller than the geometric magnification. Borghesi *et al.* [5] has performed a thorough investigation of this discrepancy. They explained this discrepancy by supposing that the point source is not located at the target plane, but at a distance x in front of the target. In this case, the magnification is M_{exp}=(L+x)/(d+x)< M_G=L/d. If one makes this assumption, the experimental magnification, M_{exp}, can be expressed as a function of the geometrical magnification, M_G, expected from a point source located at the target plane, i.e.,M_{exp}=M_G(L+x)/(L+ M_Gx), as shown in Fig. 7.3.

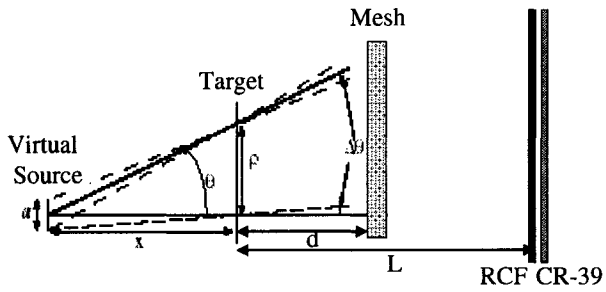

Figure 7.3: The schematic virtual source plot.

This assumption implies the smallness of the proton source, which is smaller than the laser focal spot size. This is a big advantage for radiography study because the source size is always the limitation to achieve better lithography resolution. Using the laser-driven proton accelerator can overcome this difficulty.

7.1.3 Future Work

The small-sized proton source has been observed in our experiments, and this is an advantage for radiography. However, other musts for particle beams are the small-emittance characteristic and the smaller energy spectrum spread of the proton beam. The emittance of the laser-driven proton beam still is not fully controllable because of the unclarity of the target geometry effects; no current result shows control of the proton energy spectrum. Meanwhile, the proton energy still is too low to have thicker mask radiography. All these aspects need to be resolved in order to provide a higher efficiency proton accelerator. Then a better quality proton accelerator will be achieved for future proton radiography.

7.2 Proton Radiotherapy

7.2.1 LET Advantage

Proton beams also can be used in clinical applications: proton radiotherapy. Proton beams have advantages in medical therapy. The absorption pattern of a heavy-charged-particle beam, such as the proton beam, resembles the ideal more closely than does the pattern of uncharged particle beams, such as photon beams (see Fig. 7.4). When protons enter the body, they deposit a minimal amount of energy; as they continue to traverse tissues and gradually slow down, the amount of energy they deposit per micron of travel gradually increases until they decelerate to a certain velocity. Then, suddenly, the remaining energy is given up in about a centimeter of distance. This is the Bragg Peak.

By varying the energy of the beam, the radiation oncologist can spread out the peak to encompass volumes greater than 1 cm. This essentially reverses the photon pattern so that protons build up their dose near the end of their travel. This Linear

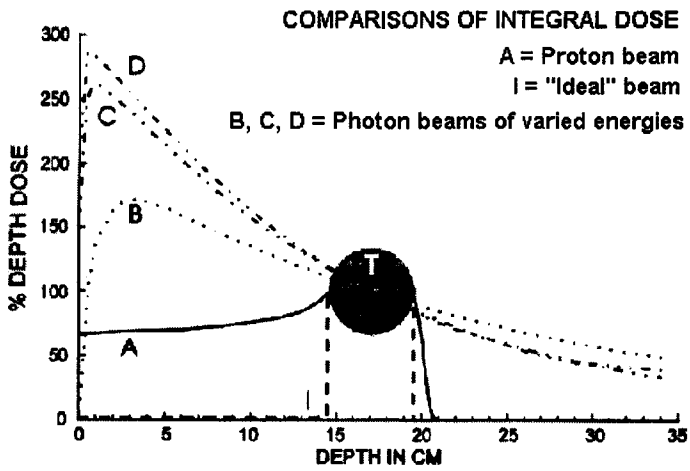

Figure 7.4: A comparison of proton, "ideal," and photon beams. The x axis is the depth under the skin; the y axis is the proton beam energy absorption percentage.

Energy Transfer (LET) is what non-destructive therapy requires.

7.2.2 Laser-Driven Proton Radiotherapy

From clinical radiography uses, proton therapy has lagged behind photon and electron beam therapy because of the prohibitively high cost of the conventional proton therapy system that is based on cyclotron or synchrotron technology. Solutions should be found for smaller, more compact, and cost-effective facilities to make proton therapy affordable and economical.

Recently, proton acceleration using laser-induced plasmas has garnered more interest. Both theoretical and experimental studies have been carried out to accelerate protons or light ions using high-power, short-pulsed lasers. These may be further developed for therapeutic applications.

Unfortunately, for proton therapy, a 250MeV close to monoenergetic proton beam is required, but the current maximum proton energy is only 60 MeV (see Fig. 7.5). For such high proton energy, a high-power (10^{21} to 10^{22} W/cm^2) laser is being acquired for laser-proton acceleration studies. On the other hand, the proton beam is

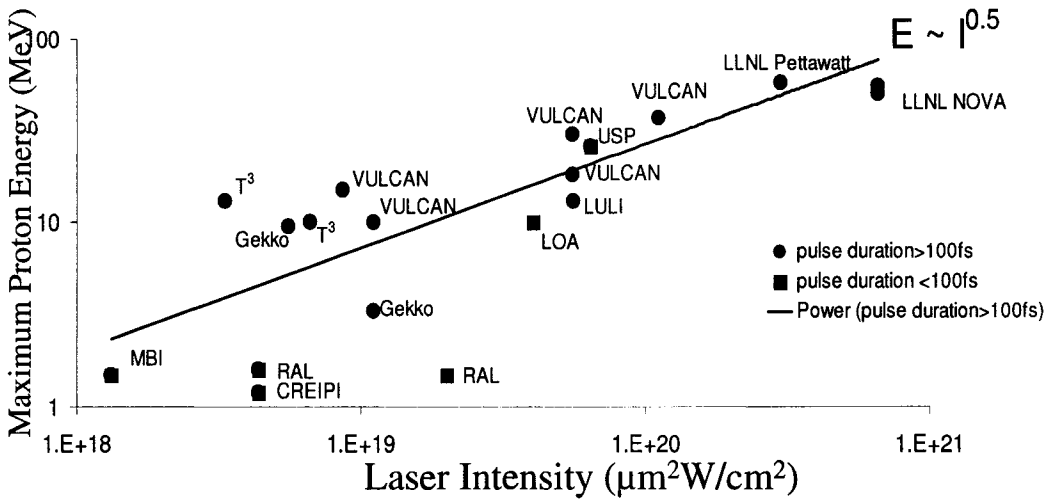

Figure 7.5: Summary plot for different institutes, showing the relationship between maximum proton energy and peak laser intensity.

not monoenergetic.

To fulfill the requirements of proton radiotherapy, further research on improvement of proton acceleration in terms of its efficiency and quality are necessary. Nevertheless, the peak intensity of the current setting has reached 10^{22} W/cm^2 [3]; the emmitance of the proton beam reached 0.004 mm-mrad [13]. The goal of laser-driven proton therapy is just around the corner.

CHAPTER VIII

Conclusion

Particle acceleration using ultrahigh-intensity laser-produced plasmas has become a very interesting area of investigation in recent years. The electrostatic field established by the charge separation from a laser-induced ponderomotive force has the ability to drive particles from plasma into a vacuum. This simple laser and plasma particle accelerator setup can significantly reduce the size and cost of the accelerator. More specifically, proton acceleration from the solid target has good prospects for various applications, which are still pending, on the invention of compact, low-cost proton accelerators. However, many of these applications would require higher proton energy production from the accelerator. For this reason, the optimization and control of laser-plasma interactions are becoming important issues at the present time.

My thesis not only illustrates the mechanism of proton acceleration by ultrahigh-intensity-laser and solid-target interaction, but also explores the method by which to control the quality of the proton beam. Three methods are discussed in the thesis, including:

(1) From the measurements of electron angular distribution, the effects and importance of the return currents, surface magnetic field, and the electrostatic field

changes are illustrated. My experimental measurements of the angular distribution of fast electrons provide a beneficial measurement to obtain the electric potential changes and magnetic field generated from the ultrahigh-laser and solid target interactions. A clear electron beam is observed at the rear side of the target; however, this electron beam did not follow the path of the ions, which is in a direction perpendicular to the solid target plate, nor did it follow the laser on-axis direction. The dependence of the deflection angle is then derived.

In addition, another clear tendency is for the electron trajectory to flow along the tangential direction of the target plate. The electron image shows that electrons are pushed from the laser-solid interaction point toward lateral extensions along the target surface. These electron distributions can indicate the electrostatic field changes inside the target plate and the magnetic field induced from the laser-plasma interactions. With the understanding of electron distribution and the prepulse optimum condition, a thorough proton acceleration mechanism was plotted.

(2) From proton acceleration in the long-plasma-scale-length solid target interaction experiment, I explored the origin of the proton source, the mechanism of proton acceleration, the spatial profile of proton beams, and the conductor and insulator targets' effects on the proton beam. From these conclusions, I developed knowledge: (a)the higher energy protons are accelerated from the rear side of the solid target; the lower energy part is from the front side; (b)the return current plays a crucial part in the solid target experiment; (c)the target thickness plays an essential role in the proton acceleration: targets thinner than half of pulse duration provide more chances for return currents to circulate and give higher proton energy output; (d)conductive targets can support smoother proton beam output than insulating targets; (e)instability-induced filamentation structure is observed. These factors can

affect the spatial and energy spectrum of the proton beam.

(3) Many previous publications have suggested that preplasma introduced by the laser prepulse is the key to affecting the efficiency of proton acceleration. However, a clear correspondence between preplasma expansion scale and proton acceleration efficiency has not yet been thoroughly investigated. My thesis provides a study of the optimization of the preplasma produced by prepulse for proton acceleration from the ultrahigh-intensity-laser and solid target interaction. A prepulse with known intensity and delayed timing was introduced by a Michelson interferometer within the laser system. The prepulse can provide the changes of plasma gradient scale length and give different preplasma scale lengths. Proton energy distribution was detected by CR-39 with layered mylar filters. Differing delay times between the main pulse and the prepulse and differing prepulse intensities were tested to obtain the correspondence between delayed time and prepulse intensity in relation to maximum proton energy. The results show that the prepulse provides tremendous influence on the proton energy. An optimum delay of the prepulse and intensity were found. Moreover, with the current laser intensity, which is 10^{22} W/cm^2, hundreds MeV proton energy protons were obtained. With such a high energy proton beam, expected applications for cancer treatment research and material science will be achieved.

My research explored improving the efficiency of proton acceleration and the mechanism involved in the movement of electrons. Specifically, the potential generated from the electrons is the key to driving the protons. My thesis has documented three factors that affect the movement of electrons: solid target materials, incident laser intensity, and the peak-to-peak contrast ratio of the laser pulse. By studying the effect of these factors, an optimum condition of the proton acceleration was achieved.

APPENDIX

APPENDIX A

Third-Order Autocorrelator

A.1 Abstract

The temporal shape of laser pulses generated from a 1.053 μm 10 terrawatt hybrid Ti:Sapphire/Nd: Phosphate glass chirped pulse amplification laser was measured by the third order autocorrelator. This appendix reports the measurement that shows an order of five differences between the intensity of the prepulse pedestal and the main pulse.

A.2 Introduction

Ultrafast lasers create optical pulses on the scale of femtoseconds (10^{-15} s), but no electronic device has a fast enough response time to resolve changes on such time scales. Third order autocorrelation, using the laser pulse, is one method to determine the temporal evolution of ultrafast pulses. The purpose of my directed study is to develop a third-order autocorrelator and measure the pulse shape of a terrawatt laser, which would be very important information for laser fusion target irradiation experiments.

Given the many stages involved in producing and amplifying ultrafast light pulses, there can be many mechanisms that can lead to an asymmetric pulse shape. Second

order autocorrelation cannot reflect these asymmetric shapes, due to the symmetric properties of the correlation function. Even so, such information is essential, since most experiments are particularly sensitive to the prepulse as opposed to the postpulse.

Third order autocorrelation, on the other hand, yields a true measurement of pulse shape, as well as a large dynamic range for pulse contrast measurements (10^7). Therefore, a third-order autocorrelator is a necessary diagnostic for an ultrafast laser.

A.3 Theory

An autocorrelator uses the principle of harmonic generation from nonlinear material to provide temporal information about the ultrafast laser pulse. The method of nonlinear mixing for the measurement of short optical pulses is well known. The intensity of the second harmonic generation (SHG) light pulse is proportional to the square of the intensity of the fundamental pulse, $I_{2\omega}(t) \propto I_{\omega}^2(t)$, and the signal-to-noise contrast of the SHG pulse is the square of the signal-to-noise contrast of the fundamental pulse. Therefore, in a frequency-tripling experiment, the SHG is a rather clean probe for measuring small precursors preceding the fundamental pulse. The third harmonic signal is given by [2]:

$$
\begin{aligned}
E_{3\omega}(\tau) &\approx G_{3\omega}(\tau) \\
&\propto \int_{-\infty}^{\infty} I_{\omega}(t) I_{2\omega}(t-\tau) dt \\
&\simeq I_{\omega}(t) \int_{-\infty}^{\infty} I_{2\omega}(t-\tau) dt
\end{aligned}
\tag{A.1}
$$

When τ is greater than the laser pulse width,

$E_{3\omega}(\tau) \approx G_{3\omega}(\tau) \approx I_{\omega}(t)$

Therefore, the intensity of the third harmonic signal is proportional to the fundamental pulse intensity distribution.

A.4 Measurement

The layout of the optics setup for the T^3 laser for the third order autocorrelation is shown in Fig. A.1.

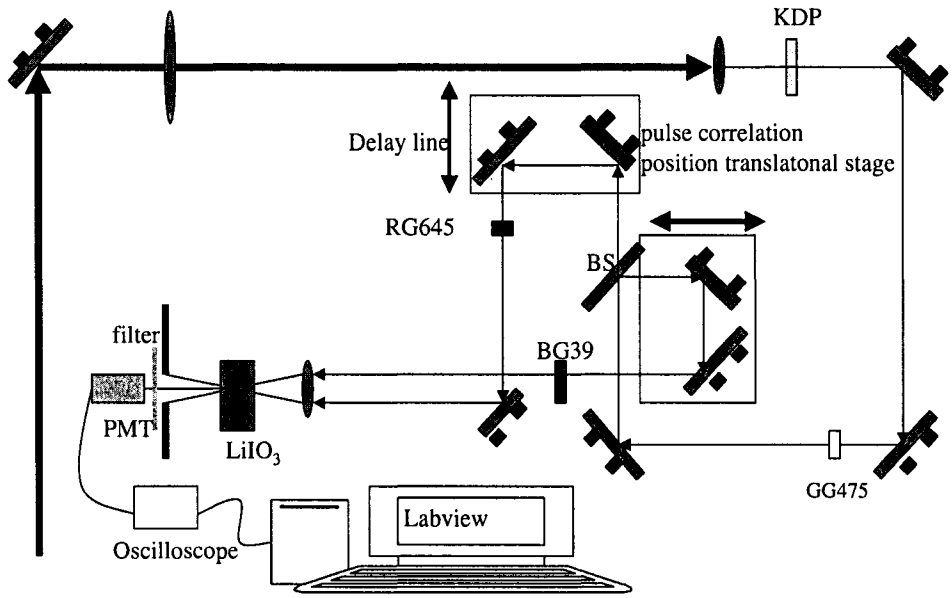

Figure A.1: Experimental setup for third order autocorrelation trace.

The laser beam starts from the left side. In order to increase the intensity of the laser at the nonlinear crystal, a demagnification telescope is installed. A 1 μm laser beam from a Ti:/Sapphire oscillator and regeneration amplifier passes through a KD*P second harmonic generation crystal. A co-directional second harmonic generation takes place inside the KD*P crystal, and then a GG475 color glass filter is installed to attenuate the fundamental pulse without decreasing the second harmonic generation signal. A 5 mm 50% glass beam splitter is used to separate the fundamental (1.053 μm) and the second harmonic (0.526μm) generation from KD*P

monic generation signal. A 5 mm 50% glass beam splitter is used to separate the fundamental (1.053 μm) and the second harmonic (0.526μm) generation from KD*P crystal.

The second harmonic generation (which is green) goes through a delay line controlled by a half-meter translational stage. This half-meter distance corresponds to about 1.67 nanoseconds in time, which is long enough for the pedestal identification and detection. The fundamental arm (which is infrared) enters an optical delay line that has a two-inch translation range for alignment purposes.

BG-39 and RG-645 are glass color filters for filtering green and infrared, respectively. Focusing these two signals onto a third harmonic generation crystal is achieved by a lens. These two beams need to be incident at symmetric positions (relative to the optics axis of the lens) in order to have the same focal positions on the tripling crystal. Lithium iodate crystal was used as the tripling crystal because of its high efficiency.

These two beams intersect at a narrow angle, which meets the phase matching condition. The third harmonic signal, at an ultraviolet wavelength of 351nm, should be in the center of these two beams. An iris is then used to cut these two beam signals and allow the third harmonic signal to pass through.

In front of the photomultiplier (PMT), used as a detector, a 2 mm glass color filter, UG-11, was inserted to contribute more to the task of filtering the UV signal. The PMT , however, needs to be calibrated to work before being used. At a fixed applied bias voltage, the PMT signal should reflect the same amount of attenuation of the ND filter when the calibrated ND filter is inserted. Finally, alignment of the long translation stage is essential; some dropping of signal tends to occur following even small misalignments.

With an automatic LabView program, a 50fs-resolution third-order autocorrelation trace can be obtained (see Fig. A.2.)

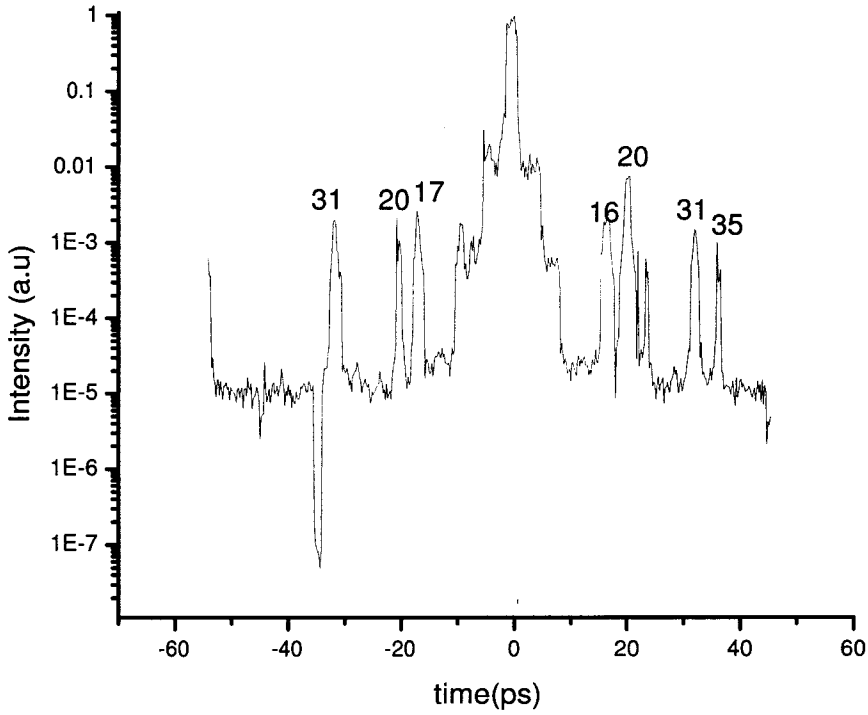

Figure A.2: Third-order autocorrelator trace of T^3 laser, July, 18, 2004.

BIBLIOGRAPHY

BIBLIOGRAPHY

[1] K. Adumi, K. A. Tanaka, T. Matsuoka, T. Kurahashi, T. Yabuuchi, Y. Kitagawa, R. Kodama, K. Sawai, K. Suzuki, K. Okabe, T. Sera, T. Norimatsu, and Y. Izawa. Characterization of preplasma produced by an ultrahigh intensity laser system. *Phys. Plasma*, 11(8):3721, August 2004.

[2] G. Albrecht. Temporal shape analysis of nd3+ : Yag active passive mode-locked pulses. *Optics Communications*, 40(1):59, 1981.

[3] S. Bahk, V. Chvykov, G. Kalintchenko, A. Maksimchuk, G. Mourou, N. Saleh, and V. Yanovsky. Generation, amplitude and phase characterization of 10/sup 21/ w/cm/sup 2/ intensity. volume 1, page 3. CLEO, IEEE, 2004.

[4] M. Borghesi, D. H. Campbell, A. Schiavi, M. G. Haines, O. Willi, A. J. Mackinnon, P. Patel, L. A. Gizzi, M. Galimberti, R. J. Clarke, F. Pegoraro, H. Ruhl, and S. Bulanov. Electric field detection in laser-plasma interaction experiments via the proton imaging technique. *Phys. of Plasma*, 9(5):2214, May 2002.

[5] M. Borghesi, A. J. Mackinnon, D. H. Campbell, D.G. Hicks, S. Kar, P. K. Patel, D. Price, L. Romagnani, A. Schiavi, and O. Willi. Multi-mev proton source investigations in ultraintense laser-foil interactions. *Phys. Rev. Lett.*, 92(5):055003, February 2004.

[6] F. Brunel. Not-so-resonant, resonant absorption. *Phys. Rev. Lett.*, 59(1):52, July 1987.

[7] S. V. Bulanov and V. S. Khoroshkov. Feasibility of using laser ion accelerators in proton therapy. *Plasma Phys. Rep.*, 28(5):453–456, 2002.

[8] V. Yu. Bychenkov, W. Rozmus, A. Maksimchuk, D. Umstader, and C. E. Capjack. Fast ignitor concept with light ions. *Plasma Phys. Rep.*, 27(12):1017–1020, 2001.

[9] V. Yu. Bychenkov, V. T. Tikhonchuk, and S. V. Tolokonnikov. Nuclear reactions triggered by laser-accelerated high-energy ions. *Sov. Phys. JETP*, 88(6):1137, 1999.

[10] E. L. Clark, K. Krushelnick, J. R. Davies, M. Zepf, M. Tatarakis, F. N. Beg, A. Machacek, P. A. Norreys, M. I. K. Santala, I. Watts, and A. E. Dangor. Measurements of energetic proton transport through magnetized plasma from intense laser interactions with solids. *Phys. Rev. Lett.*, 84(4):670, 24 January 2000.

[11] E. L. Clark, K. Krushelnick, M. Zepf, F. N. Beg, M. Tatarakis, A. Machacek, M. I. K. Santala, I. Watts, P. A. Norreys, and A. E. Dangor. Energetic heavy-ion and proton generation from ultraintense laser-plasma interactions with solids. *Phys. Rev. Lett.*, 85(8):1654, 21 August 2000.

[12] J. A. Cobble, R. P. Johnson, T. E. Cowan, N. Renard-Le Galloudec, and M. Allen. High resolution laser-driven proton radiography. *J. App. Phys.*, 92(4):1775, 15 August 2002.

[13] T. E. Cowan, J. Fuchs, H. Ruhl, A. Kemp, P. Audebert, M. Roth, R. Stephens, I. Barton, A. Blazevic, E. Brambrink, J. Cobble, J. Fernandez, J.-C. Gauthier, M. Geissel, M. Hegelich, J. Kaae, S. Karsch, G. P. Le Sage, S. Letzring, M. Manclossi, S. Meyroneinc, A. Newkirk, H. Pepin, and N. Renard-LeGalloudec. Ultralow emittance, multi-mev proton beams from a laser virtual-cathode plasma accelerator. *Phys. Rev. Lett.*, 92(20):204801, May 2004.

[14] G. I. Dudnikova, V. Yu. Bychenkov, A. Maksimchuk, G. Mourou, J. Nees, S. G. Bochkarev, and V. A. Vshivkov. Electron acceleration by few-cycle laser pulses with single-wavelength spot size. *Phys. Rev. E*, 67(7):026416, Febuary 2003.

[15] T. Feurer, W. Theobald, R. Sauerbrey, I. Uschmann, D. Altenbernd, U. Teubner, P. Gibbon, E. Forster, G. Malka, and J. L. Miquel. Onset of diffuse reflectivity and fast electron flux inhibition in 528-nm-lasersolid interactions at ultrahigh intensity. *Phys. Rev. E*, 56(4):4608, October 1997.

[16] K. Flippo. Ion beam generation from high-intensity-laser dense-plasma interactions and applications. University of Michigan, Ph.D. Dissertaion, 2004.

[17] D. W. Forslund and J. U. Brackbill. Magnetic-field-induced surface transport on laser-iradiated foils. *Phys. Rev. Lett.*, 48(23):1614, June 1982.

[18] J. Fuchs, T. E. Cowan, P. Audebert, H. Ruhl, L. Gremillet, A. Kemp, M. Allen, A. Blazevic, J.-C. Gauthier, M. Geissel, M. Hegelich, S. Karsch, P. Parks, M. Roth, Y. Sentoku, R. Stephens, and E. M. Campbell. Spatial uniformity of laser-accelerated ultrahigh-current mev electron propagation in metals and insulators. *Phys. Rev. Lett.*, 91(25):255002, December 2003.

[19] J. Fuchs, Y. Sentoku, S. Karsch, J. Cobble, P. Audebert, A. Kemp, A. Nikroo, P. Antici, E. Brambrink, A. Blazevic, E. M. Campbell, J. C. Fernandez, J.-C. Gauthier, M. Geissel, M. Hegelich, H. Pepin, H. Popescu, N. Renard-LeGalloudec, M. Roth, J. Schreiber, R. Stephens an, and T. E. Cowan. Comparison of laser ion acceleration from the front and rear surfaces of thin foils. *Phys. Rev. Lett.*, 94(4):045004, Febuary 2005.

[20] Bruce J. Gerbia and Dimitri A. Dimitroyannisb. The response of kodak edr2 film in high-energy electron beams. *Med. Phys.*, 30(10):2703, October 2003.

[21] L. Gremillet, G. Bonnaud, and F. Amiranoff. Filamented transport of laser-generated relativistic electrons penetrating a solid target. *Physics of Plasmas*, 9(3):941, March 2002.

[22] M. G. Haines. Thermal instability and magnetic field generataion by large heat flow in a plasma, especially under laser-fusion conditions. *Phys. Rev. Lett.*, 47(13):917, 28 September 1981.

[23] M. G. Haines. Saturation mechanisms for the generated magnetic field in nonuniform laser-matter irradiation. *Phys. Rev. Lett.*, 78(2):254, January 1997.

[24] G. Hairapetian and R. L. Stenzel. Particle dynamics and current-free double layers in an expanding collisionless, two-electron-population plasma. *Phys. Fluids B*, 3(4):899, April 1991.

[25] S. P. Hatchett, C. G. Brown, T. E. Cowan, E. A. Henry, J. S. Johnson, M. H. Key, J. A. Koch, A. B. Langdon, B. F. Lasinski, R. W. Lee, A. J. Mackinnon, D. M. Pennington, M. D. Perry, T. W. Philips, M. Roth, T. C. Sangster, M. S. Singh, R. A. Snavely, M. A. Stoyer, S. C. Wilks, and K. Yasuike. Electron, photon, and ion beams from the relativistic interaction of petawatt laser pulses with solid targets. *Phys. of Plasma*, 7(5):2076, May 2000.

[26] M. Honda, J. Meyer-ter-Vehn, and A. Pukhov. Collective stopping and ion heating in relativistic-electron-beam transport for fast ignition. *Phys. Rev. Lett.*, 85(10):2128, September 2000.

[27] M. Kaluza, J. Schreiber, M. I. K. Santala, G. D. Tsakiris, K. Eidmann, J. Meyer ter Vehn, and K. J. Witte. Influence of the laser prepulse on proton acceleration in thin-foil experiments. *Phys. Rev. Lett.*, 93(4):045003, July 2004.

[28] T. Kammash, K. Flippo, and D. Umstadter. Laser accelerated plasma propulsion system (lapps). In *37th AIAA/ASME/SAE/ASEE Joint Propulsion Conference and Exhibt*, 2001, page 3810, Salt Lake City, UT, 8-11 July 2001. AIAA, AIAA. paper 2001-3810.

[29] R. Kodama, P. A. Norreys, K. Mima, A. E. Dangor, R. G. Evans, H. Fujita, Y. Kitagawa, K. Krushelnick, T. Miyakoshi, N. Miyanaga, T. Norimatsu, S. J. Rose, T. Shozaki, K. Shigemori, A. Sunahara, M. Tampo, K. A. Tanaka, Y. Toyama, T. Yamanaka, and M. Zepf. Fast heating of ultrahigh-density plasma as a step towards laser fusion ignition. *Nature*, 412:798, August 2001.

[30] Willium. L. Kruer. *The Plysics of Laser Plasma Interactions.* Addison-Wesley Publishing Company, 1988.

[31] W.L Kruer and Kent Estabrook. Jxb heatimg by very intense light. *Phys. Fluids*, 28(1):430, January 1985.

[32] R. Lee and R. N. Sudan. *Phys. Fluids*, 14:1213, 1971.

[33] T. Lin, K. Flippo, M. Rever, A. Maksimchuk, and D. Umstadter. Mechanism and control of high-intensity-laser-driven proton beams. In *Advanced Accelerator Concepts: Eleventh Workshop*, volume 737, page 595. AIP, June 2004.

[34] W. H. Lowdermilk and J. E. Murray. The multipass amplifier: theory and numerical analysis. *J. Appl. Phys.*, 51:2436, January 1980.

[35] A. J. Mackinnon, Y. Sentoku, P. K. Patel, D. W. Price, S. Hatchett, M. H. Key, C. Andersen, R. Snavely, and R. R. Freeman. Enhancement of proton acceleration by hot-electron recirculation in thin foils irradiated by ultraintense laser pulses. *Phys. Rev. Lett.*, 88(21):215006, 27 May 2002.

[36] A. Maksimchuk, S. Gu, K. Flippo, and D. Umstadter. Forward ion acceleration in thin films driven by a high-intensity laser. *Phys. Rev. Lett.*, 84(18):4108, 1 May 2000.

[37] Y. Murakami, Y. Kitagawa, Y. Sentoku, M. Mori, R. Kodama, K. A. Tanaka, K. Mima, and T. Yamanaka. Observation of proton rear emission and possible gigagauss scale magnetic fields from ultra-intense laser illuminated plastic target. *Phys. of Plasmas*, 8(9):4138, September 2001.

[38] Tatsufumi Nakamura, Susumu Kato, Hideo Nagatomo, and Kunioki Mima. Surface magnetic field and fast electrons current layer formation by ultra-intense laser irradiation. *Phys. Rev. Lett.*, 93(26):265002, 2004.

[39] K. Nemoto, A. Maksimchuk, S. Banerjee, K. Flippo, G. Mourou, D. Umstadter, and V. Yu. Bychenkov. Laser-triggered ion acceleration and table top isotope production. *App. Phys. Lett.*, 78(5):596, 29 January 2001.

[40] Dwight R. Nicholson. *Introduction to Plasma Theory.* John Wiley and Sons, 1983.

[41] P. A. Norreys, A. P. Fews, F. N. Beg, A. R. Bell, A. E. Dangor, P. Lee, M. B. Nelson, H. Schmidt, M. Tatarakis, and M. D. Cable. Neutron production from picosecond laser irradiation of deuterated targets at intensities of 10^{19} w cm^{-2}. *Plasma Phys. Control. Fusion*, 40:175–182, 1998.

[42] Yasuaki Okano, Yoichiro Hironaka, Kazutaka G. Nakamura, Ken ichi Kondo, Yuji Oishi, Takuya Nayuki, and Koshichi Nemoto. Energy distribution of electrons ejected from a copper target in a femtosecond laser field of 10^{17} w/cm^2. *JOURNAL OF APPLIED PHYSICS*, 95(5):2278, March 2004.

[43] Luis Plaja and Luis Roso. Analytical description of a plasma diffraction grating induced by two crossed laser beams. *Phys. Rev. E*, 56(6):7142, December 1997.

[44] G. Pretzler. *Phys. Rev. E*, 58:1165, 1998.

[45] M. Roth, A. Blazevic, M. Geissel, T. Schlegel, T. E. Cowan, M. Allen, J.-C. Gauthier, P. Audebert, and J. Fuchs. Energetic ion generated by laser pulses: A detailed study on target properties. *Phys. Rev. Spec. Top. Accel. and Beams*, 5:061301, 2002.

[46] M. Roth, T. E. Cowan, M. H. Key, S. P. Hatchett, C. Brown, W. Fountain, J. Johnson, D. M. Pennington, R. A. Snavely, S. C. Wilks, K. Yasuike, H. Ruhl, F. Pegoraro, S. V. Bulanov, E. M. Campbell, M. D. Perry, and H. Powell. Fast ignition by intense laser-accelerated proton beams. *Phys. Rev. Lett.*, 86(3):436, January 2001.

[47] Y. Sentoku, V. Y. Bychenkov, K. Flippo, A. Maksimchuk, K. Mima, G. Mourou, Z. M. Sheng, and D. Umstadter. High-energy ion generation in interaction of short laser pulse with high-density plasma. *Appl. Phys. B*, 74:207–215, February 2002.

[48] Y. Sentoku, T. E. Cowan, A. Kemp, and H. Ruhl. High energy proton acceleration in interaction of short laser pulse with dense plasma target. *Physics of Plasmas*, 10(5):2009–2015, May 2003.

[49] Y. Sentoku, K. Mima, Z. M. Sheng, P. Kaw, K. Nishihara, and K. Nishikawa. Three-dimensional particle-in-cell simulations of energetic electron generation and transport with relativistic laser pulses in overdense plasmas. *Phys. Rev. E*, 65:046408, March 2002.

[50] Y. Sentoku, H. Ruhl, K. Mima, R. Kodama, K. A. Tanaka, and Y. Kishimoto. Plasma jet formation and magnetic-field generation in the intense laser plasma under oblique incidence. *Phys. Plasma*, 6(7):2855, July 1999.

[51] Z.-M. Sheng, K. Mima, Y. Sentoku, M. S. Jovanovic, T. Taguchi, J. Zhang, and J. Meyer-ter-Vehn. Stochastic heating and acceleration of electrons in colliding laser fields in plasma. *Phys. Rev. Lett.*, 88(4):055004, Febuary 2002.

[52] Z.-M. Sheng, K. Mima, Y. Sentoku, K. Nishihara, and J. Zhang. Generation of high-amplitude plasma waves for particle acceleration by cross-modulated laser wake fields. *Phys. Plasma*, 9(7):3147, July 2002.

[53] Luis O. Silva, Michael Marti, Jonathan R. Davies, Ricardo A. Fonseca, Chuang Ren, Frank S. Tsung, and Warren B. Mori. Proton shock acceleration in laser-plasma interactions. *Phys. Rev. Lett.*, 92(1):015002, January 2004.

[54] R. A. Snavely, M. H. Key, S. P. Hatchett, T. E. Cowan, M. Roth, T. W. Philips, M. A. Stoyer, E. A. Henry, T. C. Sangster, M. S. Singh, S. C. Wilks, A. Mackinnon, A. Offenberger, D. M. Pennington, K. Yasuike, A. B. Langdon, B. F. Lasinski, J. Johnson, M. D. Perry, and E. M. Campbell. Intense high-energy proton beams from petawatt-laser irradiation of solids. *Phys. Rev. Lett.*, 85(14):2945, October 2000.

[55] D. Strickland and G. Mourou. Compression of amplified chirped optical pulses. *Opt. Commun.*, 56:219, 1985.

[56] Max Tabak, James Hammer, Michael E. Glinsky, William L. Kruer, Scott C. Wilks, John Woodworth, E. Michael Campbell, and Michael D. Perry. Ignition and high gain with ultra-powerful lasers. *Phys. Plasma*, 1(5):1626, May 1994.

[57] M. Tatarakis, A. Gopal, I. Watts, F. N. Beg, A. E. Dangor, K. Krushelnick, U. Wagner, P. A. Norreys, E. L. Clark, M. Zepf, and R. G. Evans. Measurements of ultrastrong magnetic fields during relativistic laserplasma interactions. *Phys. of Plasmas*, 9(5):2244, May 2002.

[58] U. Teubner, K. Eidmann, U. Wagner, U. Andiel, F. Pisani, G. D. Tsakiris, K. Witte, J. Meyer-ter-Vehn, T. Schlegel, and E. Forster. Harmonic emission from the rear side of thin overdense foils irradiated with intense ultrashort laser pulses. *Phys. Rev. Lett.*, 92(18):185001, May 2004.

[59] Z. -M. Sheng, Y. Sentoku, K. Mima, J. Zhang, W. Yu, and J. Meyer-ter-Vehn. Angular distributions of fast electrons, ions, and bremsstrahlung x/g-rays in intense laser interaction with solid targets. *Phys. Rev. Lett.*, 85(25):5340, December 2000.

[60] D. Umstadter, S.-Y. Chen, A. Maksimchuk, G. Mourou, and R. Wagner. Nonlinear optics in relativistic plasmas and laser wake field acceleration of electrons. *Science*, 273:472, 1996.

[61] K. B. Wharton, C. D. Boley, A. M. Komashko, A. M. Rubenchik, J. Zweibeck, J. Crane, G. Heys, T. Cowan, and T. Ditmire. Effects of nonionizing prepulses in high-intensity laser-solid interactions. *Phys. Rev. E*, page 025401(R), July 2001.

[62] S. C. Wilks, W. L. Kurer, M. Tabak, and A. B. Langden. Absorption of ultra-intense pulses. *Phys. Rev. Lett.*, 69(9):1383, August 1992.

[63] S. C. Wilks, A. B. Langdon, T. E. Cowan, M. Roth, M. Singh, S. Hatchett, M. H. Key, D. Pennington, A. Mackinnon, and R. A. Snavely. Energetic proton generation in ultra-intense laser-solid interactions. *Phys. Plasmas*, 8(2):542, February 2001.

[64] Ping Zhang, Ned Saleh, Shouyuan Chen, Zhengming Sheng, and Donald Umstadter. An optical trap for relativistic plasma. *Phys. of Plasmas*, 10(5):2093, May 2003.

[65] Y. Zhu, A. S. Kirov, V. Mishra, A. S. Meigooni, and J. F. Williamson. Quantitative evaluation of radiochromic film response for two-dimensional dosimetry. *Med. Phys.*, 24(2):223, February 1997.